DIPLOMARBEIT

Directional Microphone based on Artificial Spider Silk

Design and Fabrication of Bio-Inspired Acoustic Airflow Sensors

zur Erlangung des akademischen Grades
Diplom-Ingenieur/in
im Rahmen des Studiums
066 460 Physikalische Energie- und Messtechnik
eingereicht von

Thomas Tropper
Matrikelnr.: 1225832

ausgeführt am Institut für Sensor- und Aktuatorsysteme
der Fakultät für Elektrotechnik und Informationstechnik der Technischen Universität Wien

Betreuung
Betreuer/in: **Univ.Prof. Dr. Silvan Schmid**
Mitwirkung: **Univ.Ass. Miao-Hsuan Chien**

Wien, 02.09.2021

(Unterschrift Verfasser/in)

(Unterschrift Betreuer/in)

Abstract

Directional sound detection is usually achieved by using pressure microphone arrays. The drawback of such arrays is that they need further signal processing and show difficulties in combining high sensitivity, flat bandwidth and compactness. To counter these disadvantages spider silk microphones have shown to be very efficient at capturing the fluctuations in air velocity with a figure-of-eight directivity, high sensitivity and a broad frequency response [1, 2, 3]. To create an artificial sensor based on this concept, silicon nitride (SiN_x) was used. Even though the SiN_x-samples have a high pre-stress they show high sensitivity and in average a figure-of-eight characteristic. In combination with a laser vibrometer it was shown that this setup is a fully functioning microphone. Yet there is plenty of space for improvement. Reduction in internal stress and a portable transduction setup are upcoming challenges for SiN_x-fiber sensors.

Contents

1. Introduction

Many applications take advantage of directional sound detection whether it is used for sound source localization or noise filtering like in hearing aids. This is usually accomplished by using arrays of omni-directional pressure microphones. These consist of at least two microphones measuring the sound pressure at different locations before the different arrival times are processed to locate the direction of the source. Even though this technique is used in most applications, it appears to have difficulties fitting broad bandwidth, high sensitivity and directional response into compact sensor requirements [1, 2, 3].

Several bio-inspired solutions have been discovered to solve these difficulties. For instance many animals have the ability of sensing fluctuations in their surrounding medium using fine sensory hairs. Measuring the particle velocity instead of sound pressure offers the advantage of measuring the directional information with only one sensor element and avoids unnecessary processing time. Unfortunately, artificial hair sensors cannot keep up with their biological counterparts when it comes to the ability to sense airflow at their resonance frequency efficiently. In addition to that they do not provide a broad bandwidth of flat frequency response [1, 3].

Recent discoveries have shown that spiders can use their silk to measure acoustic airflow. Sufficiently thin fibers of spider silk have shown to follow along in the movement of the surrounding airflow with maximum efficiency ($v_{air}/v_{silk} \sim 1$) over a broad frequency range (1 Hz–50 kHz). This is due to the strong viscous forces acting on the fiber overpowering the internal forces of the string [1]. Further investigations have shown that these highly damped nanofibers naturally provide a figure-of-eight directivity pattern along their bandwidth (100 Hz–10 kHz) [2].

State-of-the-art advancements use highly-damped 2D meshes of artificial Polymethylmethacrylate (PMMA) nanofibers. These 8 mm × 8 mm meshes show ultra high broadband sensitivity and figure-of-eight directionality by using the same principle as investigated using spider silk [3]. Further advancements are trying to build sensor concepts based on thin porous plates or thin beams, since the fabrication of nanodimensional fibrous structures is still not as sophisticated as the fabrication of thin films [4].

In consideration of mentioned advantages, it is of great interest to develop a procedure to fabricate such artificial spider silk fibers to make them marketable. This thesis examines silicon nitride (SiN_x) nanofibers in their fabrication and physical behavior to create a spider silk inspired microphone.

2. Theory

Since the geometry and the readout concept of the string resonator suggests that only the displacement and velocity perpendicular to the surface of the sensor matters, an one-dimensional description for the sensor's theory is adequate.

2.1. Drag Force Driven and Damped Resonator

An oscillating object in a medium will be affected by the linear drag force when the system's Reynolds number is small enough ($Re < 2200$) [5]. The linear drag force or viscous resistance is:

$$F_{drag} = -cv \tag{1}$$

The magnitude of the force is directly proportional to the velocity v. c is a constant which is dependent on the properties of the surrounding medium and the system's geometry. Since both a moving system and a moving medium cause a viscous resistance, the final force experienced is determined by the residual velocity of the resonator $\frac{dz}{dt}$ and its surrounding fluid v_m.

$$cv_r(t) = c\Big[v_m(t) - \frac{dz}{dt}(t)\Big] \tag{2}$$

This force can be split in two parts. One describes the damping applied to the system by the medium:

$$F_{damping} = -c\frac{dz}{dt}(t) \tag{3}$$

The other force is the driving force acting on the resonator due to a moving fluid:

$$F_{driving} = cv_m(t) \tag{4}$$

Hence the equation of motion for this system is:

$$m\frac{d^2}{dt^2}z + c\frac{d}{dt}z + kz = \underbrace{cv_m(t)}_{F(t)} \tag{5}$$

The general solution for a driven damped harmonic oscillator is already given by:

$$z(t) = \underbrace{\frac{F_0/m}{\sqrt{(\Omega^2 - \omega^2)^2 + 4\zeta^2\Omega^2\omega^2}}}_{|z_0|} cos(\omega t + \varphi) \tag{6}$$

Using (see B.2)

$$F(t) = \underbrace{c\omega\xi_0}_{F_0} e^{i\omega t} \tag{7}$$

with the mediums displacement amplitude ξ_0 the solution is:

$$z(t) = \frac{c\omega\xi_0/m}{\underbrace{\sqrt{(\Omega^2-\omega^2)^2+4\zeta^2\Omega^2\omega^2}}_{|z_0|}} cos(\omega t+\varphi) \tag{8}$$

This can be rearranged to display the ratio between driving force particle displacement and the resonators response displacement:

$$\frac{|z_0|}{\xi_0} = \frac{c\omega/m}{\sqrt{(\Omega^2-\omega^2)^2+4\zeta^2\Omega^2\omega^2}} \tag{9}$$

Using the relations for the damping coefficient $n_c = \frac{c}{2m}$ and the damping ratio $\zeta = \frac{n_c}{\Omega}$ the equation can be rewritten as

$$\frac{|z_0|}{\xi_0} = \frac{2\zeta\Omega\omega}{\sqrt{(\Omega^2-\omega^2)^2+4\zeta^2\Omega^2\omega^2}}. \tag{10}$$

Assuming $|v_0| = |z_0|\cdot\omega$ and $v_m = \xi_0\cdot\omega$ the relation between driving and system velocity is equivalent.

$$\frac{|z_0|}{\xi_0} = \frac{|v_0|}{v_m} \tag{11}$$

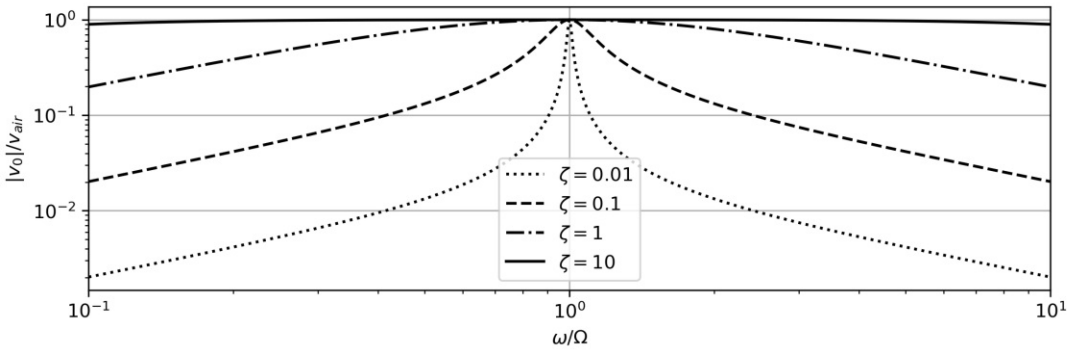

Fig. 2.1 Ratio between system velocity $|v_0|$ and air particle velocity $v_m = v_{air}$ for increasing values of ζ.

So according to (10) and Fig. 2.1 systems with higher damping ratio ζ can follow the

velocity of the driving medium more efficiently around their eigenfrequency Ω.

2.2. Nanomechanical Model

2.2.1. Drag Force on Dish-String Models

Stoke's law describes the drag force acting on spherical and dish-like objects exposed to the laminar flow of a viscous fluid. The viscous force acting perpendicular to the surface of the dish

$$F_{dish} = 16 r \mu v_r \tag{12}$$

depends on its radius r, the dynamic viscosity μ of the surrounding fluid and the relative velocity v_r between the dish and the fluid. Since there is no closed-form solution for string- and beam-like objects, a close enough approximation can be made by picturing a string as an array of dishes [5]. A dish-string model of length L would consist of $n = \frac{L}{2r}$ dishes with a total drag force of

$$F_{string} = n \cdot 16 r \mu v_r = 8 L \mu v_r \tag{13}$$

and hence a force per unit length of

$$dF_{string} = \underbrace{8\mu}_{C} v_r \cdot dx. \tag{14}$$

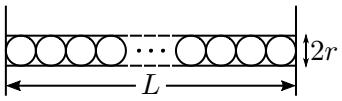

Fig. 2.2 Dish-string model of n dishes.

2.2.2. Spider Silk Fiber Model

A simplified model to describe the equation of motion for an unstressed, doubly-clamped fiber of spider silk was suggested in the paper "Sensing fluctuating airflow with spider silk" [1]:

$$E I_y \frac{\partial^4 u(x,t)}{\partial x^4} + \rho A \frac{\partial^2 u(x,t)}{\partial t^2} = C v_r(t) + M \frac{dv_r(t)}{dt} \tag{15}$$

The mechanical bending force per unit length is given by the Young's modulus E and the area moment of inertia $I_y = \pi d^4/64$. The second term on the left-hand side describes

the inertia of the fiber with its cross-section $A = \pi d^2/4$ and the density of the fiber ρ. On the right-hand side of the equation there is the drag force term followed by the force of added mass, both depending on the relative velocity between air and string motion $v_r(t) = v_{air}(t) - \frac{\partial u(x,t)}{\partial t}$, with C as damping factor and $M = \frac{1}{2}\rho_{air}A$ as added mass. Since all the terms on the left side are strongly dependent on the diameter of the fiber, for sufficiently thin fibers they will lose significance and the right-hand side will clearly dominate the system.

$$0 \approx Cv_r(t) + M\frac{dv_r(t)}{dt}. \tag{16}$$

2.2.3. Silicon Nitride Fiber Model

In thin film structures usually tensile stress occurs due to the fabrication process. Doubly-clamped structures like strings therefore are stressed by default. Bending the string will result in a restorative force acting against the displacing force depending on the angle of the unit length. For sufficiently long strings the force applied by intrinsic tensile stress is way higher than the force applied by the beam's thickness and thus can be dropped from the equation. In comparison to Eq. (16) the added-mass term was also dropped. This is due to the relatively low density of air (around $1.2\,\mathrm{kg/m^3}$) in relation to the density of silicon nitride (around $3000\,\mathrm{kg/m^3}$). Finally a simplified description for the silicon nitride fiber is given by

$$-\sigma A\frac{\partial^2 u(x,t)}{\partial x^2} + \rho A\frac{\partial^2 u(x,t)}{\partial t^2} = Cv_r(t) \tag{17}$$

where $u(x,t)$ can be split in a time dependent part $u(t)$ and a positional part $\phi(x) = \sum_i^\infty \phi_i(x)$, which is the sum of all possible mode shapes. The interacting forces between fiber and air on the right side of the equation are separated in an internal and an external part. The internal part joins the left side as a damping term while the external part remains the driving force of the system.

$$\rho A\frac{\partial^2 u(x,t)}{\partial t^2} + C\frac{\partial u(x,t)}{\partial t} - \sigma A\frac{\partial^2 u(x,t)}{\partial x^2} = Cv_{air}(t) \tag{18}$$

By using effective parameters, it is possible to simplify the continuum mechanical system down to a lumped element model. Therefore, each term of the equation needs to be transformed with Galerkin's method [6]. For Eq. (19) Galerkin's method was applied on

the undriven equation:

$$\frac{\partial^2 u(t)}{\partial t^2} + \underbrace{\frac{C}{\rho A}}_{2n_c} \frac{\partial u(t)}{\partial t} + \underbrace{\frac{\sigma}{\rho}\beta_n^2}_{\Omega_n^2} u(t) = 0 \tag{19}$$

Finally the damping ratio $\zeta = \frac{n_c}{\Omega}$ using $\beta_n = \frac{n\pi}{L}$ can be determined by

$$\zeta = \frac{C}{2n\pi}\frac{L}{A}\frac{1}{\sqrt{\sigma\rho}}. \tag{20}$$

As shown in (10) maximizing the damping ratio will result in a larger frequency range of flat response around the system's eigenfrequency Ω.

3. Methods

3.1. Sample Design

The design of a sensor concept turns out to be challenging. While deriving the physical boundaries for a successful sensor can be straightforward, the technical boundaries of the available facility can be a limiting factor. The goal is to find the overlap of what works on paper and of what can actually be achieved with modern technology.

3.1.1. Physical Boundaries

Several nanomechanical sensor concepts try to achieve high quality factors and thus very low damping ratios, which can mostly be reached in ultra high vacuum. The concept of an acoustic nanomechanical velocity sensor is exactly the opposite. In the best case scenario the sensor should only move when the surrounding air moves. Hence a high damping ratio is essential.

The idea is to create a fiber fine enough to follow along the movement of the surrounding air particles as efficiently as possible. Therefore the damping ratio ζ of the SiN_x fiber needs to be maximized. Looking at (20), it can be observed that the damping ratio of the fiber scales with the dynamic viscosity μ_{air} and the total length of the fiber L. Hence maximizing the length of the string is an option, since the dynamic viscosity cannot be directly influenced. In contrast, the formula suggests to keep the string's cross-section A and its internal properties, density ρ and tensile stress σ, as low as possible.

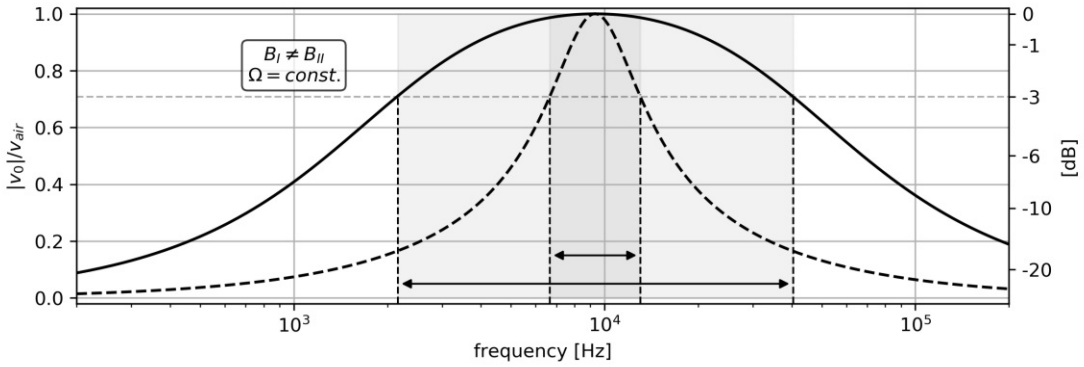

Fig. 3.1 Effect of damping on bandwidth B.

Fig. 3.1 and Fig. 3.2 were plotted using (10) to visualize how changes in the system's parameters affect bandwidth B and eigenfrequency Ω.

In Fig. 3.1 an increasing bandwidth can be observed for decreasing cross-sections of the string. Since the eigenfrequency Ω is not dependent on the cross-section for sufficiently long strings, the bandwidth is not shifted. The same effect can be seen when changing to fluids with higher dynamic vicosity μ. On the other hand, changing the string's properties like length L or internal tensile stress σ will result in a tuning of the system's eigenfrequency Ω. (see Fig. 3.2)

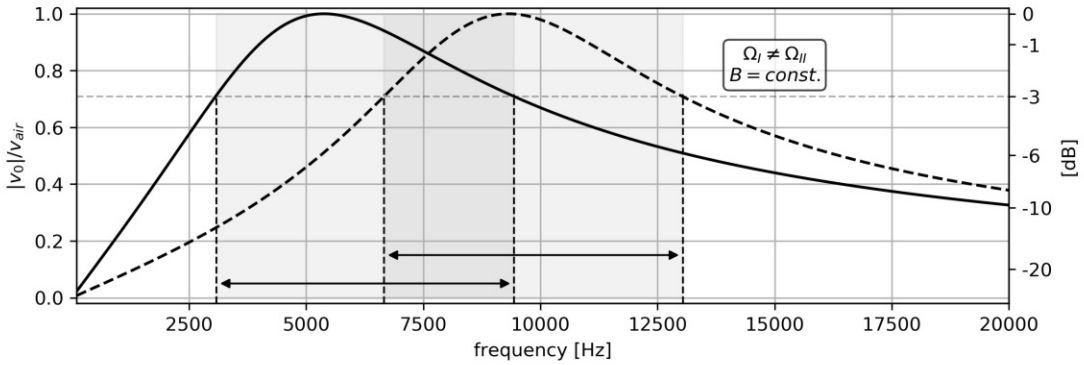

Fig. 3.2 Tuning of string Ω.

Since the materials density ρ is present in both the damping coefficient n_c and eigenfrequency Ω, changes in density will result in changes for bandwidth and eigenfrequency.

3.1.2. Technical Boundaries

Especially during the fabrication process the real difficulties and limitations of the sample design becomes apparent. This is reflected in the low yield of eight samples from initially 50 samples on the wafer. Most difficulties arise in the release of the samples. Very long strings (∼6–20 mm) designed to sense the low density and low viscosity flow of air tend to break under the comparably high density of the KOH-release. Each string has to be released separately using tweezers to keep the sample's orientation parallel to the stream when removing them from the KOH-bath. As described in the laboratory protocol (3.2), this could be avoided by prematurely stopping the etching process and subsequently applying a dry-etching process using Xenondifluoride(XeF_2)-etching.

3.2. Fabrication

The masks for silicon nitride (SiN_x) and KOH were designed using the CleWin software and subsequently sent to fabrication with the following specifications:

- 5“×5“-mask
- low reflective chromium
- defect density $0.5/\mathrm{cm}^2$
- minimum dimension $\geq 1\,\mu\mathrm{m}$

For the fabrication a <100> silicon wafer, with nominal thickness of 380 µm and a layer of SiN_x (LPCVD) on both sides with nominal thickness of 300 nm was used. Even though wafers with thinner layers of SiN_x are available and in theory are in fact better for the sensitivity of the sensor, the thicker wafer was used for the first attempts, since a thicker wafer material gives more stability to the samples and thus a higher yield can be achieved.

Step 1: Wafer Cleaning with isopropyl alcohol and a megasonic wafer cleaner.

Step 2: Frontside Lithography using an image reversal resist (AZ5214 E).

Pre-bake wafer at 120°C to get rid of the residual humidity on the substrate.

Spin-coating of photo resist (AZ5214 E) on wafer with 3000 rpm for 40 s to equally distribute the resist on the wafer surface. The residual rotation of the spinner was used to guide a tissue with acetone around the edges of the wafer to prevent the photo resist to accumulate.

Soft-bake wafer on heat plate for 5 min at 107°C, leaving some residual humidity left in the resistor. This is needed for the photo reaction of the resist.

Light exposure with photo mask for 3 s with vacuum contact for a sharp contrast.

Reverse -bake the mask for 2 min at 120°C to change the resist type to negative.

Illuminate wafer without photo mask for 35 s.

Rinsing the wafer with developer (AZ MIF726).

Step 3: Physical Vapor Deposition (PVD) of a 100 nm chromium layer with electron beam vaporization at 8×10^{-8} mbar.

Step 4: Lift Off of chromium on the places without resist to structure the etching mask. Different levels of acetone baths and ultrasonic shaking. Isopropyl alcohol and ultrasonic shaking. Finish with megasonic wafer cleaner.

Step 5: Reactive Ion Etching (RIE) of SiN_x on wafer surface for 8 min, 3 sccm O_2, 30 sccm CF_4, 150 W, 50 mTorr.

Step 6: Chromium Etching with Technietch Cr01, 1 min at room temperature and rinsing with DI-Water.

Step 7: Backside Lithography

Protection-resist spinned on frontside with 3000 rpm.

Pre-bake at 107°C with separator.

Backside cleaning with spin-coater using acetone and isopropyl alcohol.

Photoresist spin-coating of AZ6624 at 3000 rpm, 40 s + edge cleaning with acetone.

Soft-bake on heat plate at 107°C for 5 min.

Illumination of backside with photo mask for 9 s at vacuum contact.

Rinsing wafer for 18 s with developer (AZ MIF726).

Step 8: Reactive Ion Etching (RIE) of SiN_x layer on wafer backside in parallel plate etcher to create a mask for KOH etching for 8 min, 3 sccm O_2, 30 sccm CF_4, 150 W, 50 mTorr.

Step 9: Resist Strip

Acteone bath and ultrasonic cleaner.

Isopropyl alcohol bath and ultrasonic cleaner.

Megasonic wafer cleaner.

Step 10: KOH-Etching at 44% KOH, at 80°C: Backside KOH-etching (Frontside protected from acid) of 370 µm from total 380 µm of wafer thickness in 8 h and 40 min. Rinse with purified water.

Step 11: Splitting samples with a diamond cutter.

Step 12: KOH-Etching at 44% KOH, 80°C:

Single Sample Etching for 17 min, just enough to leave a thin safety layer of silicon underneath the string. Then rinse with purified water

Step 13: Xenondifluoride-Etching to remove the safety underneath the string with dry-etching.

Pre-bake sample at 150°C for 15 min to remove residual humidity, preventing hydrofluoric acid development.

7-cycle treatment for 5 s each at 5.3 mbar pressure, 0 s delay, N_2 0 sccm.

3.3. Samples

The fabrication yielded ten samples from which two did not survive further handling. Hence samples are labeled from 1 to 7 and 9 (also see C.1).

The table Tab. 1 shows the geometry of each sample in length L, width w and height h as they are sketched out in Fig. 3.3. The density of SiN_x ρ and the intrinsic tensile stress σ are given by the wafer material.

Measurements have shown that the resonance frequency f_r of sample ws19-1-9 is very low at ∼3300 Hz, although it should rather be more than 50000 Hz. Observations under an optical microscope also show visible motions of the string actuated by breathing or by the clean room ventilation. This means the sample was clearly damaged by the fabrication process. Comparing Fig. 3.5, picturing an intact clamping at both ends, with Fig. 3.6, picturing the broken anchor, the damage becomes obvious. Yet it is still a functioning string with very low tensile stress. This results in a higher damping ratio and thus is also included in the measurements. Although it has to be mentioned, that the fabrication of this string is not reproducible.

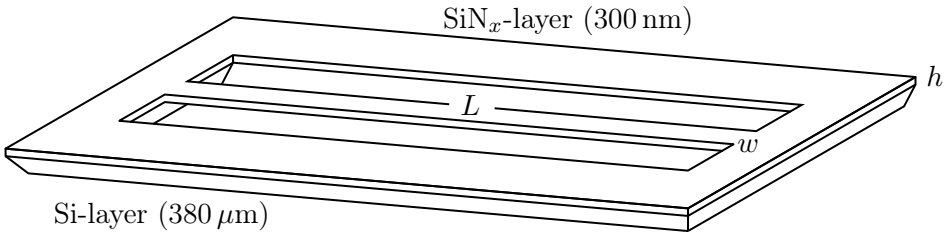

Fig. 3.3 Sample geometry and dimensions.

Tab. 1 Calculated string properties for each sample.

id	L [mm]	w [μm]	h [nm]	A [m^2]	ρ [$\frac{g}{cm^3}$]	σ [MPa]	f [Hz]	ζ	f_r [Hz]
1	12	∼4	300	1.2e-12	3.17	150	9064	0.33	7987
2	12	∼3	300	9e-13	3.17	150	9064	0.45	7037
3	10	∼3	300	9e-13	3.17	150	10876	0.37	9255
4	6	∼3	300	9e-13	3.17	150	18127	0.22	17203
5	10	∼3	300	9e-13	3.17	150	10876	0.37	9255
6	10	∼3	300	9e-13	3.17	150	10876	0.37	9255
7	10	∼3	300	9e-13	3.17	150	10876	0.37	9255
9	2	∼2	300	6e-13	3.17				∼3300

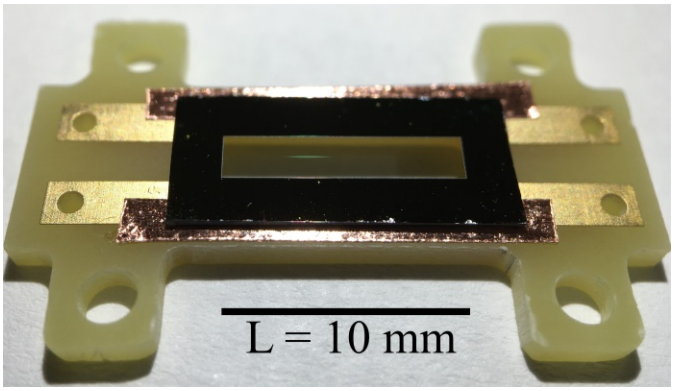

Fig. 3.4 ws19-1-3: Light reflecting on 3 µm wide string.

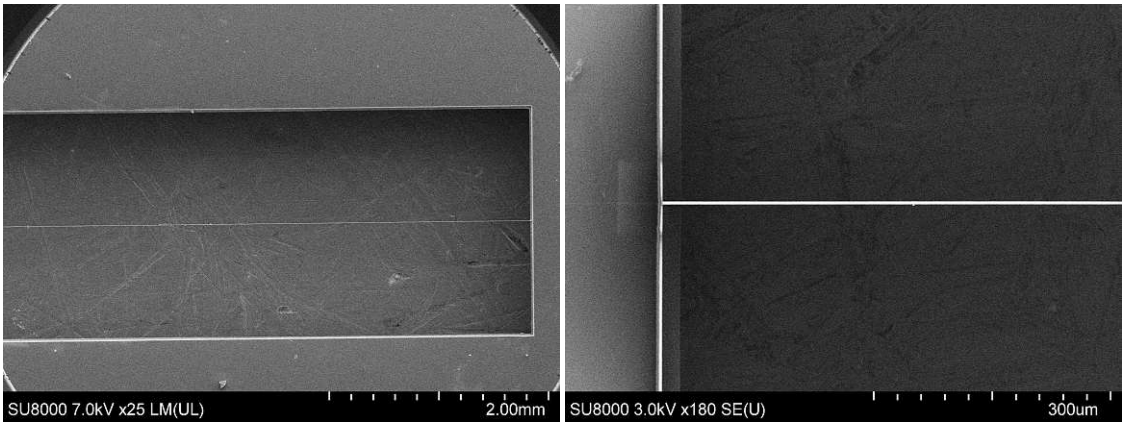

Fig. 3.5 ws19-1-1: 2×12 mm window with string (left). Intact anchor (right).

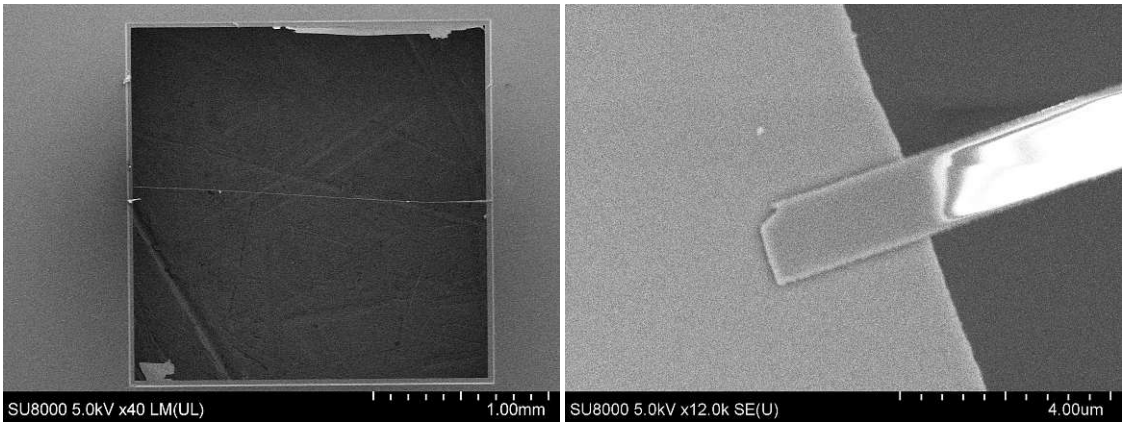

Fig. 3.6 ws19-1-9: 2×2 mm window with low stress string (left). Broken anchor still attached to frame (right).

4. Measurements

In this chapter a series of experiments is discussed, which will define the different properties of the samples like sensitivity and directivity. This however will prove to be difficult, since the readout of the samples is bound to the Micro System Analyzer (MSA). The risk to destroy any of the few samples by a gold layer deposition for an electromechanical readout is too high, since this includes abrasive processes. Unfortunately, this will

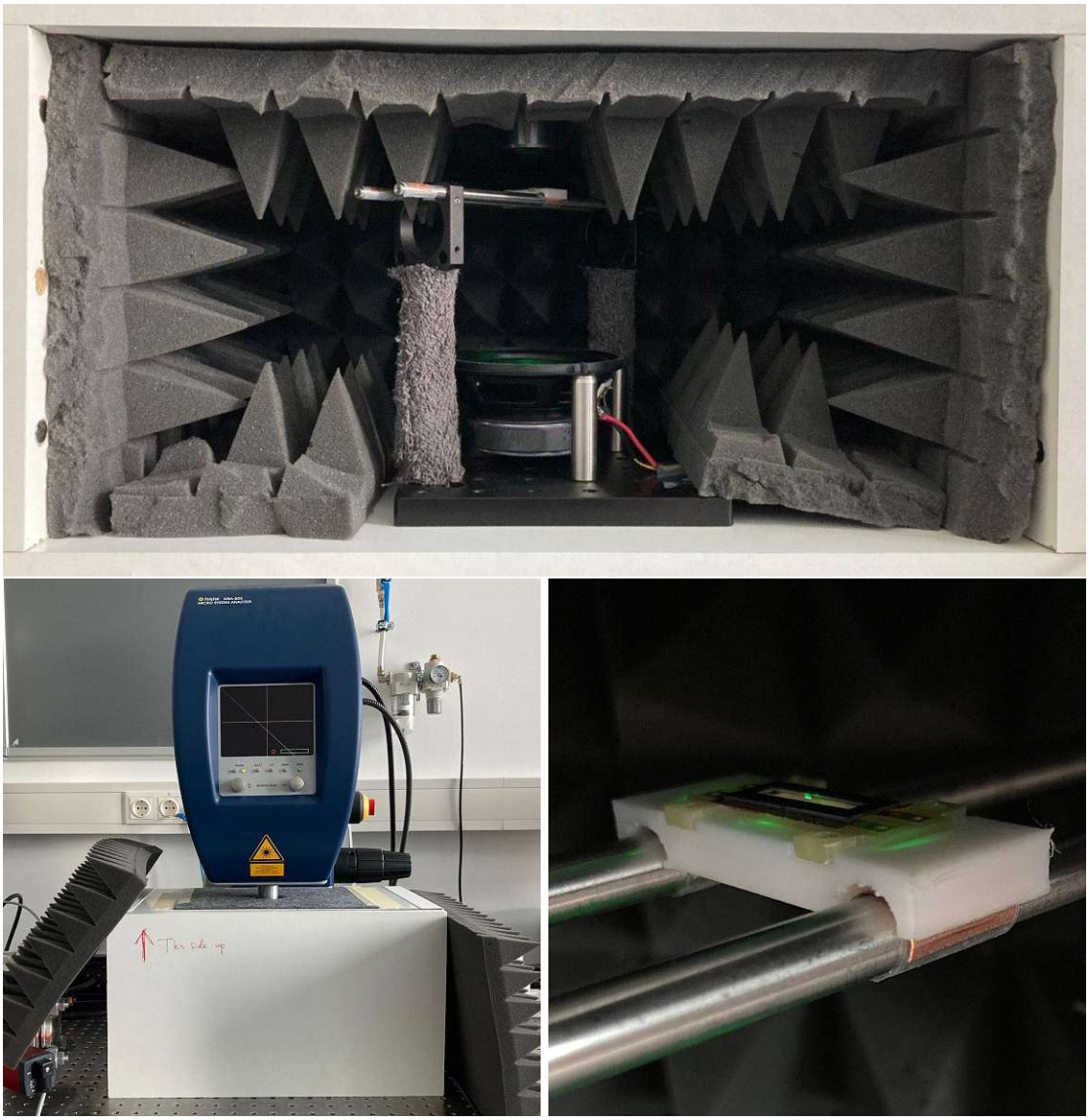

Fig. 4.1 Experimental setup with partially sound absorbing box.

prevent the setup from using an anechoic chamber, which would reduce the interference of reflected and standing waves. Nevertheless, certain characteristics can be defined for the samples.

Measurements have been made at the MSA using the velocity decoder VD09-50mm/s/V, which is relevant for the translation between the strings' velocity and the measured voltage. The samples where placed in a partially sound absorbing box, surrounded by acoustic foam panels (Fig. 4.1). A frame with optical gear was built to hold the samples between the objective of the MSA and the actuating loudspeaker (Visaton FR 10). The distance between speaker and sample was around 70 mm. In addition, there is a hole on the top of the box to lower the objective to working distance. For the experiments in sensitivity, SNR (Signal to Noise Ratio) and THD (Total Harmonic Distortion) both time signal and frequency domain have been measured, using an 1 kHz sine wave actuation with a SPL (Sound Pressure Level) of ∼94 dB (1 Pa) at the samples' position. Fig. 4.2 shows a conceptional depiction of how the strings are actuated by a speaker and measured with the laser vibrometer.

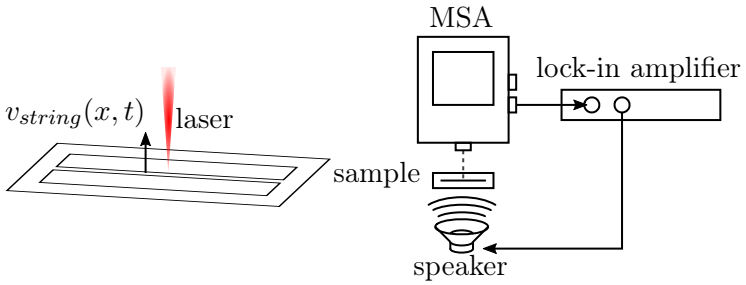

Fig. 4.2 Concept of experimental setup.

4.1. Sensitivity

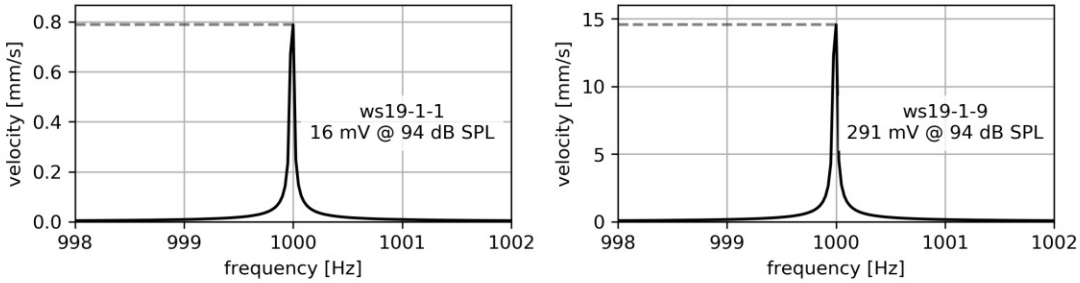

Fig. 4.3 Sensitivity of sample ws19-1-1 and ws19-1-9 @ 94 dB @ 1 kHz.

Sensitivity describes the proportion between input and output amplitude. The sensitivity was measured with an 1 kHz sine wave input signal using 94 dB SPL +/-1 dB (1 Pa) at the sample's location. The sensitivity of the microphone is equal to the peak voltage at 1 kHz and typically expressed as mV/Pa or mV @ 94 dB [7].

All samples have been measured within the experimental setup at 93.1 dB @ 1 kHz using the velocity decoder VD09-50mm/s/V. The results of the measurements can be seen in Tab. 2.

Sensitivity can vary depending on the laser's position on the string, which can be seen in the first two columns, representing two individual measurements at 1 kHz. This is a unique problem using the Micro System Analyzer, since the position of the laser beam is not always in the center of the string. Nevertheless, the magnitude of the measurements does not change and the variations are low. In addition there are further columns to describe the sensitivity for other input waves.

Tab. 2 Sensitivity @ 94 dB SPL +/-1 dB. Standardized @ 1 kHz with VD09-50mm/s/V.

Sample ID	@ 1 kHz [mV]	@ 1 kHz [mV]	@ 2 kHz [mV]	@ 3 kHz [mV]	@ 4 kHz [mV]
ws19-1-1	16 mV	14 mV	121 mV	44 mV	178 mV
ws19-1-2	14 mV	16 mV	135 mV	46 mV	192 mV
ws19-1-3	15 mV	14 mV	120 mV	41 mV	162 mV
ws19-1-4	2 mV	9 mV	73 mV	26 mV	89 mV
ws19-1-5	14 mV	14 mV	304 mV	63 mV	68 mV
ws19-1-6	10 mV	6 mV	49 mV	17 mV	64 mV
ws19-1-7	6 mV	9 mV	69 mV	25 mV	98 mV
ws19-1-9	291 mV	245 mV	1238 mV	243 mV	596 mV

4.2. Signal-to-Noise Ratio

Signal-to-Noise ratio, short SNR, is defined as the ratio of the measured signal power and the measured noise power. Alternatively, the SNR can be calculated by using the root-mean-square of the signal's amplitude. In microphone characterization the SNR is typically expressed in dB [8].

$$\begin{aligned} SNR &= \frac{P_{signal}}{P_{noise}} = \left(\frac{u_{(rms)signal}}{u_{(rms)noise}}\right)^2 \\ SNR_{dB} &= 10 \cdot log_{10}\left(\frac{P_{signal}}{P_{noise}}\right) = 20 \cdot log_{10}\left(\frac{u_{(rms)signal}}{u_{(rms)noise}}\right) \end{aligned} \tag{21}$$

To prevent harmonics from interfering with the calculation of the SNR, the noise level has been measured independently. Afterwards, the sensor was actuated with a 1 kHz sine wave at 94 dB SPL. Tab. 3 shows the SNR for different frequency domains. Specifying the frequency domain is important to keep the data comparable with other data sources. In comparison, a modern MEMS microphone has around 64 dB SNR within a bandwidth of 20 Hz-8 kHz [9].

Tab. 3 Signal-to-Noise ration within different frequency domains.

Sample ID	0–2 kHz	0–8 kHz	0–20 kHz
ws19-1-1	76.8 dB (4.82e7)	81.2 dB (1.32e8)	83.4 dB (2.17e8)
ws19-1-2	78.4 dB (6.97e7)	82.8 dB (1.93e8)	84.1 dB (2.58e8)
ws19-1-3	76.4 dB (4.34e7)	81.0 dB (1.27e8)	82.9 dB (1.94e8)
ws19-1-4	72.2 dB (1.65e7)	77.2 dB (5.29e7)	77.3 dB (5.41e7)
ws19-1-5	77.0 dB (4.98e7)	81.6 dB (1.45e8)	84.4 dB (2.76e8)
ws19-1-6	68.8 dB (7.58e6)	73.9 dB (2.46e7)	75.5 dB (3.58e7)
ws19-1-7	72.7 dB (1.87e7)	77.3 dB (5.33e7)	79.1 dB (8.1e7)
ws19-1-9	95.7 dB (3.75e9)	96.2 dB (4.21e9)	96.7 dB (4.67e9)

4.3. Total Harmonic Distortion

$$\begin{aligned} THD &= \frac{\sum_{n=1}^{5} P_n}{P_f} = \frac{\sum_{n=1}^{5} u_n^2}{u_f^2} \\ THD_{\%} &= \left(\frac{\sum_{n=1}^{5} P_n}{P_f}\right) \cdot 100 \\ THD_{dB} &= 10 \cdot log_{10}\left(\frac{\sum_{n=1}^{5} P_n}{P_f}\right) \\ THD_{\%audio} &= \frac{\sqrt{\sum_{n=1}^{5} u_n^2}}{u_f} \end{aligned} \tag{22}$$

THD is a quantization for how strongly the output signal is distorted by the harmonics of the input signal. As can be observed in Fig. 4.4 and Fig. 4.5, the fundamental mode at the actuation frequency of 1 kHz shows several harmonics with different amplitudes. Due to the sensor concept, even numbered harmonics are naturally lower, since the laser of the MSA is aiming to measure the exact middle of the sample. There are several different definitions of how the total harmonic distortion can be calculated. Since all of them have their justification, the most frequent ones were mentioned [8, 10].

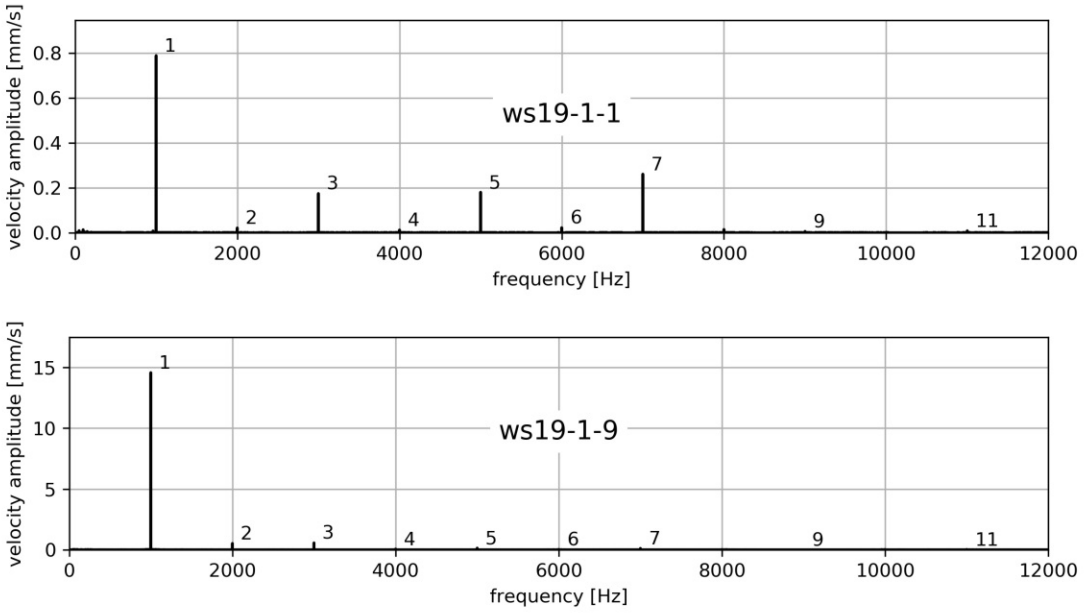

Fig. 4.4 Harmonics of ws19-1-1 and ws19-1-2 at an 1 kHz sine wave actuation.

Tab. 4 Harmonics at 2-, 3-, 4-, 5- and 6-times driving frequency (top).
Harmonics at 3-, 5-, 7-, 9- and 11-times driving frequency (bottom).

Sample ID	THD	$THD_{\%}$	THD_{dB}	$THD_{\%audio}$
ws19-1-1	0.2121	21.21%	-6.7 dB	0.46
ws19-1-2	0.1016	10.16%	-9.9 dB	0.32
ws19-1-3	0.1666	16.66%	-7.8 dB	0.41
ws19-1-4	0.7895	78.95%	-1.0 dB	0.89
ws19-1-5	0.1193	11.93%	-9.2 dB	0.35
ws19-1-6	0.1691	16.91%	-7.7 dB	0.41
ws19-1-7	0.3027	30.27%	-5.2 dB	0.55
ws19-1-9	0.0017	0.17%	-27.7 dB	0.04
ws19-1-1	0.0014	0.14%	-28.4 dB	0.038
ws19-1-2	0.0006	0.06%	-32.1 dB	0.025
ws19-1-3	0.002	0.2%	-27.0 dB	0.045
ws19-1-4	0.0054	0.54%	-22.7 dB	0.073
ws19-1-5	0.0001	0.01%	-39.0 dB	0.011
ws19-1-6	0.001	0.1%	-29.9 dB	0.032
ws19-1-7	0.0022	0.22%	-26.7 dB	0.046
ws19-1-9	0.0	0.0%	-46.8 dB	0.005

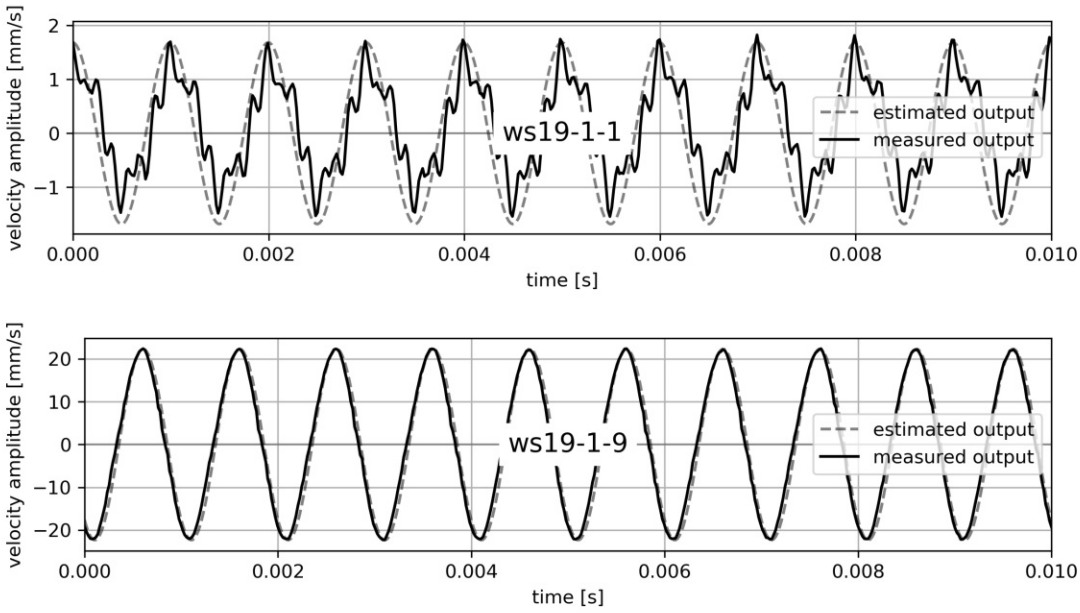

Fig. 4.5 Total harmonic distortion in ws19-1-1 and ws19-1-9.

4.4. Frequency Response

The frequency response determines how the sensor behaves along the defined frequency range. Microphones in general are expected to provide a certain flatness along the bandwidth depending on their field of application. Displaying the frequency range in dB makes it easy to classify areas of flatness with a tolerated variation of +/-1 dB [8].

The frequency domain of each sample, as well as the domain of the speaker itself, has been measured using a frequency sweep within the supported range of the speaker (80 Hz - 20 kHz). All curves have been normalized to their power at 1 kHz. After that the frequency response for each sample was divided by the speaker's frequency response.

Unfortunately, none of the samples show a significant frequency bandwidth flatness across the observed spectrum. In addition to that, the data seems to show an interaction between the sample and the measurement setup up to around 1 kHz. Hence it is difficult to classify the frequency bandwidth in which human talking is supposed to be detected (see C.3).

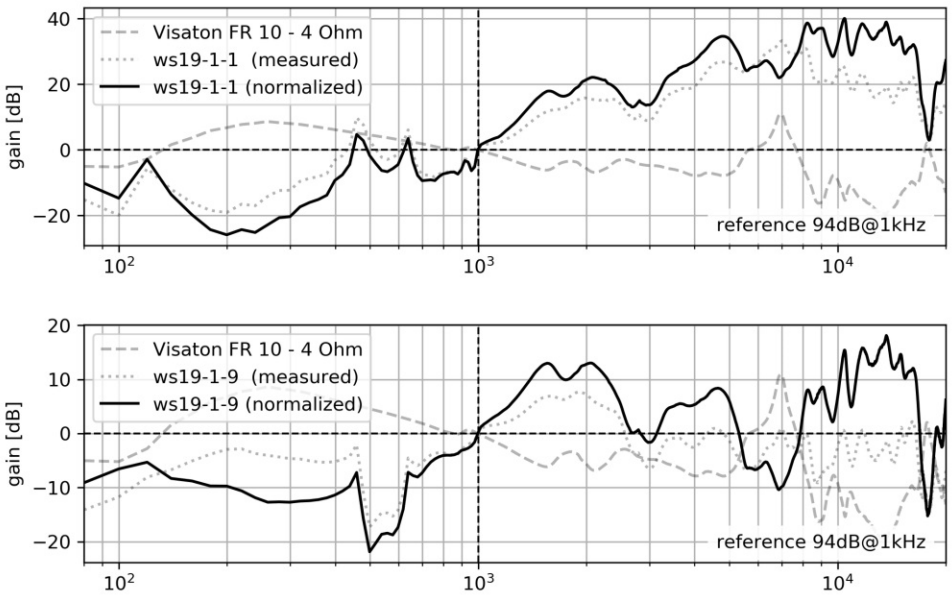

Fig. 4.6 Frequency response of ws19-1-1 and ws19-1-9.

4.5. Directionality

The directional selectivity is one of the most interesting characteristics of a microphone. It gives insight into how the microphone will react to actuation from different angles and thus determines its best application opportunities. Usually, a microphone's directionality is measured in an anechoic chamber. This reduces unwanted effects like reflections and standing waves. Since the analysis of these samples is bound to the Micro System Analyzer, the experiment is limited to less space and worse environmental interference.

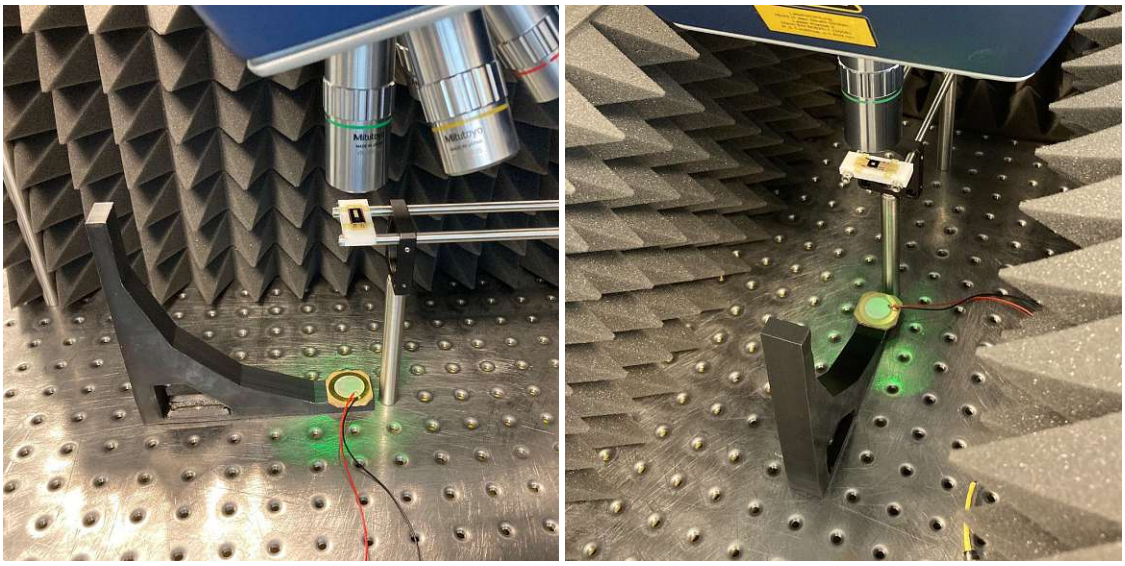

Fig. 4.7 Setup for directional selectivity experiment.

To test the sample within the limited space of the MSA, the sample is fixed with optical gear underneath the MSA-objective. A 3D-printed holder with an inner radius of 125 mm was designed to hold a piezo-buzzer in five actuation-angles ($\theta = 0°$, 22.5°, 45°, 67.5°, 90°). The holder was fixed tightly at the front and could be turned to actuate the sample from different angles ($\phi = 0°$, 45°, 90°) in the xy-plane of the optical table. To generate data for the chosen samples (2, 3, 4, 7, 9), which are all representatives for their geometry, any combination of (ϕ, θ) was actuated with a linear frequency sweep from 20 Hz to 20 kHz. The whole setup is displayed in Fig. 4.7.

For an ideal non-directional microphone the response should be independent of the

actuation angles. Hence its mathematical description

$$\begin{aligned} x &= sin(\theta)cos(\phi) \\ y &= sin(\theta)sin(\phi) \\ z &= cos(\theta) \end{aligned} \tag{23}$$

with the response factor r ideally will always be $r = \sqrt{x^2 + y^2 + z^2} = 1$. Since the samples where designed to show no response in either x- or y-direction $(x, y = 0)$, the theoretical response factor r is $r(\theta) = cos(\theta)$. This means the samples' theoretical response is 1 at $\theta = 0°$ and 0 at $\theta = 90°$.

The predicted outcome of the experiment is cosine-dependent and marked with a dashed line in Fig. 4.8 for each plot. After calculating the mean value for each spectrum at (ϕ, θ), the values were plotted and averaged for each sample. In this depiction all the samples show a clear tendency to behave according to the prediction. Of course an ideal behavior was not expected within the bottleneck at the 0%-amplitude, since reflection and scattering effects are difficult to eliminate completely.

The measured spectra show frequency dependent variations in strength and alignment of the predicted directional effect. This was made visible in Fig. C.6–C.7 by subtracting the direct actuation spectrum at θ_0 with the mean reference spectrum θ_r, with r = 22.5°, 45°, 67.5°, 90°. This leads to a graphic where values above the zero line are symbolizing the frequency areas with the predicted directional effect, while values underneath the zero line show the inverted effect. This indicates that even though the mean frequency dependency turned out to fit the prediction, there are areas at certain frequencies which actually have a higher response than the direct actuation θ_0. A reasonable explanation has not been examined yet, but since most of the problematic areas are present in all samples, these effects might be due to external influences. Reflections and standing waves at certain angles are not controllable for the chosen setup.

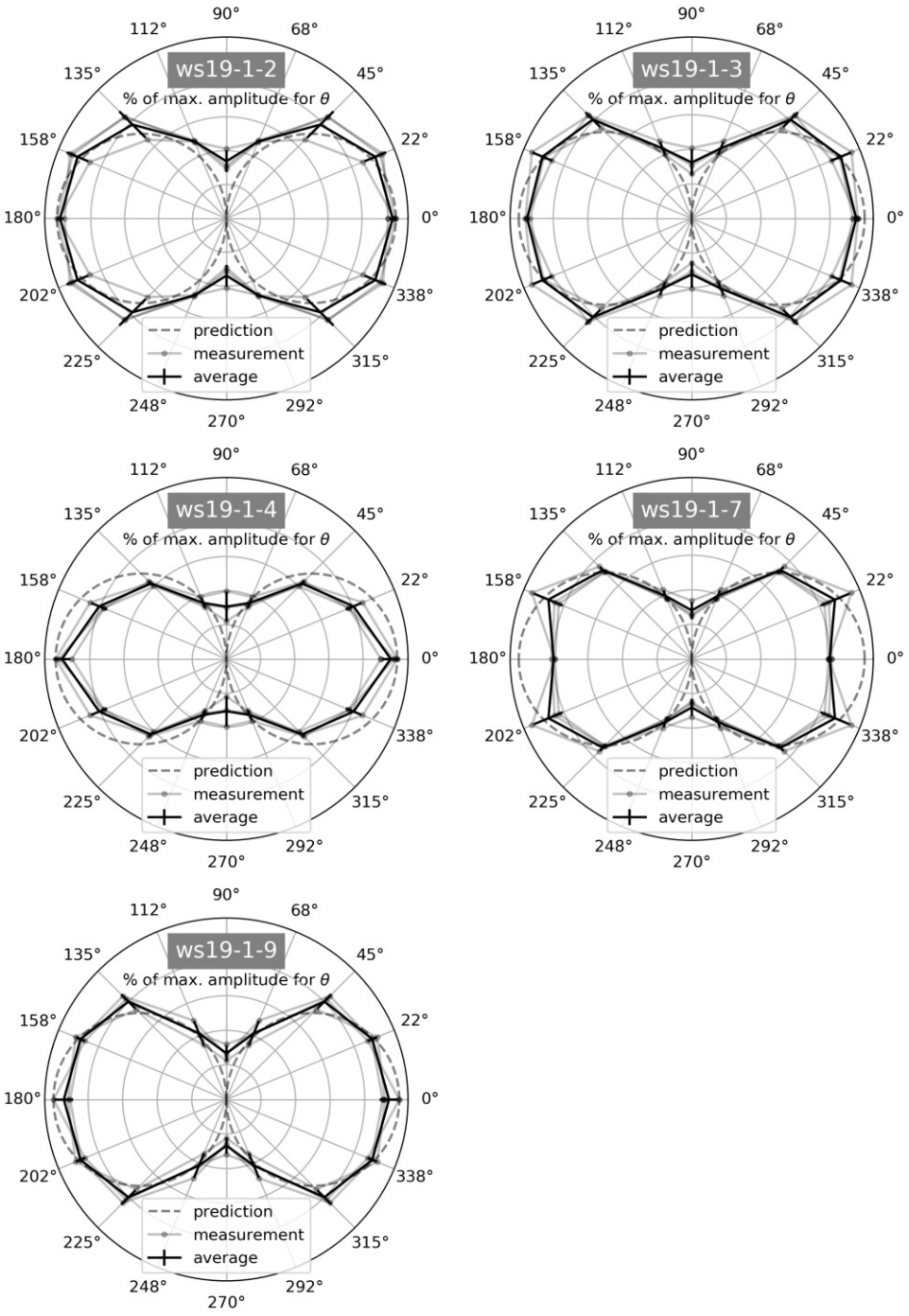

Fig. 4.8 Mean directional response for each sample calculated over the full measurement bandwidth (20 - 20000 Hz).

4.6. Recording

The ability of the sensors to work as a microphone is shown in Fig. 4.9 and Fig. 4.10. The signal has been recorded by using the Micro System Analyzer with the velocity decoder VD06-1mm/s/V at the maximum laser power of 200 µW. All samples show a high response to vocal actuation (see C.5).

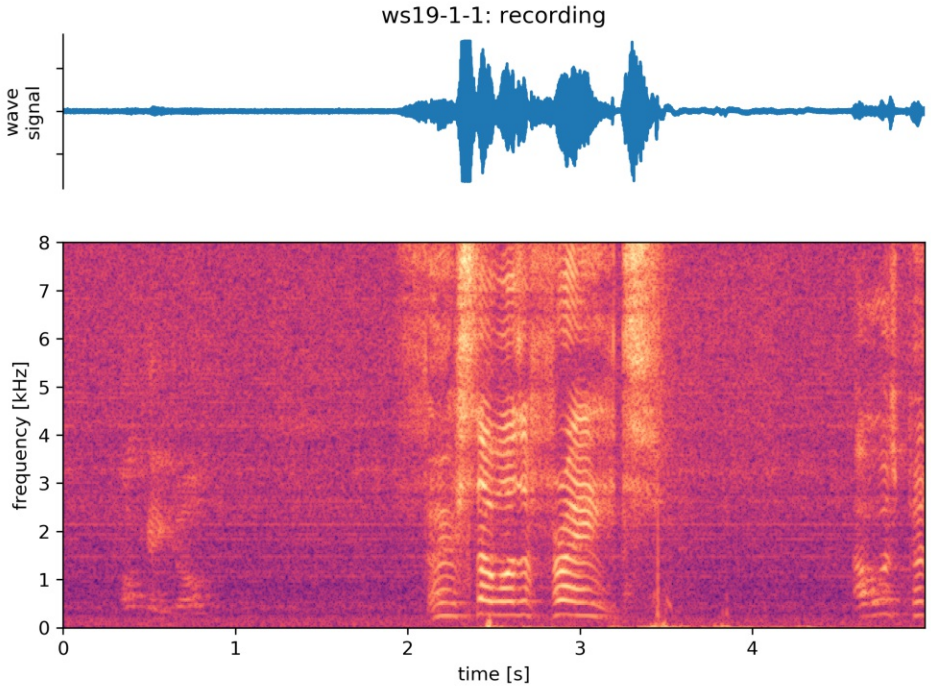

Fig. 4.9 Sonogram of a recording featuring talking at a low responsive angle of the microphone until the first second of the recording and a clear impression of the song "I Will Survive" (by Gloria Gaynor) singing :"First I was afraid" from 2–3.5 s by Niklas Luhmann.

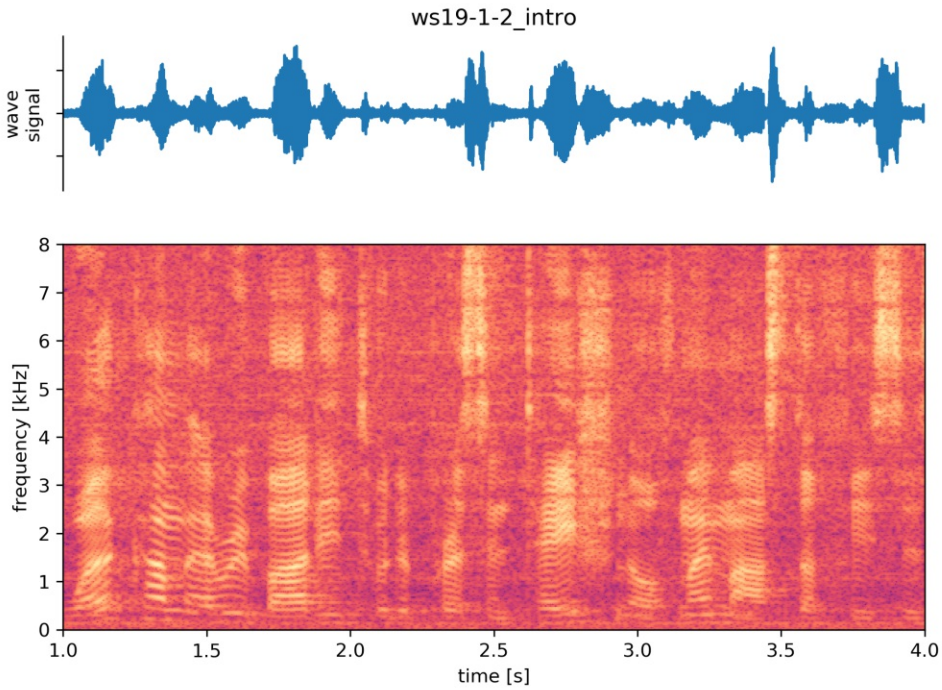

Fig. 4.10 Sonogram of a recording with ws19-1-2 saying: "Welcome everybody to the presentation of my master thesis."

5. Conclusion and Outlook

In summary, the experiments have proven that silicon nitride (SiN_x) nanostrings are capable of measuring acoustic airflow as inspired by spider silk. Still, they work in a slightly different way. While the experiments using spider silk used unstressed fibers [1, 2, 3], SiN_x-structures suffer from internal tensile stress. This results in a less effective transduction and smaller bandwidths. Nevertheless, the theoretical description of the developed strings suggests possible improvements to maximize their efficiency by minimizing the cross-section of the string and lowering the internal tensile stress.

High sensitivity and a low signal-to-noise ratio are the main attributes of the SiN_x-nanostrings. These are important features when it comes to microphone characteristics. This is reflected by the clearly audible recordings of human speech.

Unfortunately, the experiments have not shown viable data regarding the frequency response. While microphones are expected to show a flat frequency response in their functional area, the experiments could not find sufficiently flat areas in the frequency domain of the samples. This is assumed to be due to the problematic experimental setup. Since the experiment was not instrumented in an anechoic chamber, interference with reflected or standing waves cannot be excluded.

Apart from that, the measurements have shown directional selectivity. Although the directional response of the samples is not consistent along the measured frequency domain, the mean data follows the mathematical prediction. These inconsistencies are also expected to be due to environmental interference.

Future research should consider an improvement regarding the experimental environment. Eliminating sources of interference should be the main goal to improve the quality of data to better understand how such structures behave when exposed to acoustic airflow. Since acoustic testing facilities are not easy to implement in an already existing laboratory, a portable setup should be considered. This can be realized by changing the readout mechanism of the samples to an electromechanical readout concept.

As recommended above, the performance of the nanostrings can be improved by decreasing the strings cross-section and lowering internal tensile stress. The latter can be done by an oxygen plasma treatment [11].

In conclusion, this concept shows potential be implemented in applications where directional sound detection along a broad frequency range is necessary. This sensor type could improve hearing aids, speech recognition and even be used in human defense applications. Until then, this concept warrants further investigation.

A. Lumped Element Model

The lumped element model is a simplification of the continuum mechanical system.

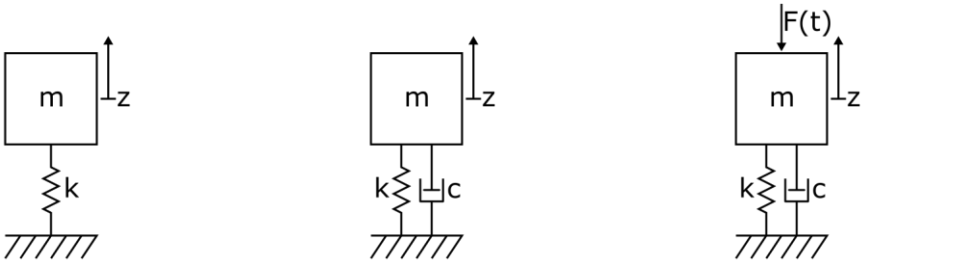

$m\frac{d^2}{dt^2}z = -kz$ $\quad$ $m\frac{d^2}{dt^2}z = -c\frac{d}{dt}z - kz$ $\quad$ $m\frac{d^2}{dt^2}z = -c\frac{d}{dt}z - kz + F(t)$

(a) Undamped oscillator. **(b)** Damped oscillator. **(c)** Driven resonator.

Fig. A.1 Three stages of lumped element models.

A.1. Free Harmonic Oscillator

The free harmonic oscillator (Fig. A.1a) resembles an ideal oscillating system without any external or internal interference. Newton's second law and Hook's law theoretically would keep the system oscillating ad infinitum at its eigenfrequency of

$$\Omega = \sqrt{\frac{k}{m}} \tag{24}$$

with spring constant k and mass m [12].

A.2. Damped Harmonic Oscillator

A damped harmonic oscillator (Fig. A.1b) is a more realistic approach at describing an oscillating system by taking damping forces like friction in viscous media into account. Hence the oscillation of the system will show a decreasing amplitude over time. How the system reacts to the damping force depends on the damping coefficient

$$n_c = \frac{c}{2m} \tag{25}$$

where c is the damping factor, which can be dependent on the system's geometry and the properties of the surrounding medium. Another way to characterize the damping

force on the system is by calculating the damping ratio

$$\zeta = \frac{n_c}{\Omega}, \tag{26}$$

which sets the damping coefficient n_c in relation to the system's eigenfrequency Ω. Solving the equation of motion for a damped harmonic oscillator

$$\frac{d^2}{dt^2}z + \underbrace{\frac{c}{m}}_{2n_c}\frac{d}{dt}z + \underbrace{\frac{k}{m}}_{\Omega^2} z = 0 \tag{27}$$

using the Ansatz

$$z(t) = z_0 e^{\gamma t} \tag{28}$$

ultimately leads to three different cases of damped systems depending on the damping coefficient.

$$\gamma_{1,2} = -n_c \pm i\sqrt{\Omega^2 - n_c^2} \tag{29}$$

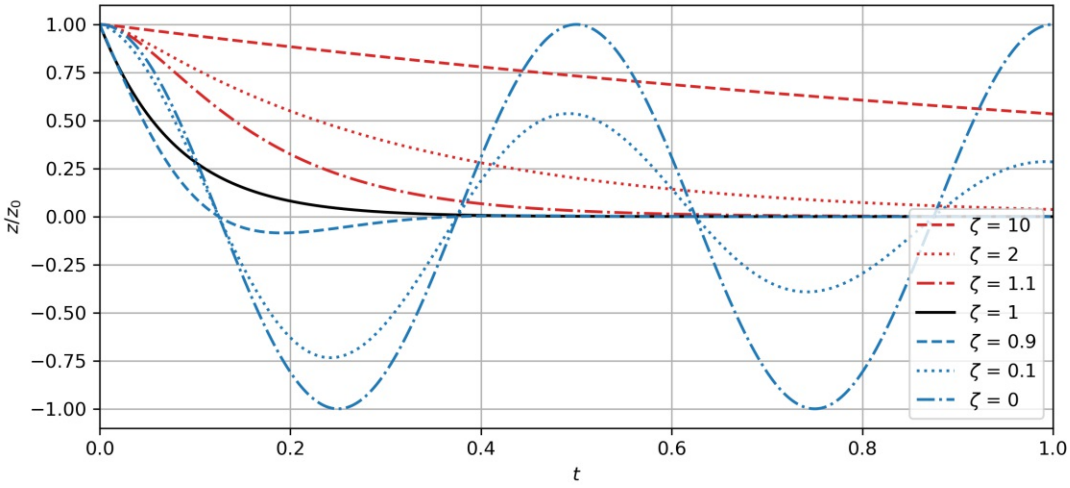

Fig. A.2 A 2 Hz oscillation with different damping ratios ζ. Over-critical damping in red. Critical damping in black. Under-critical damping in blue.

A.2.1. Under-Critically Damped System ($n_c < \Omega$, $\zeta < 1$)

In an under-critically damped system the damping coefficient is smaller than the eigenfrequency and hence the value of the square root term becomes imaginary

$$\gamma_{1,2} = -n_c \pm i \underbrace{\Omega\sqrt{1-\zeta^2}}_{\omega_0}. \tag{30}$$

The physically relevant solution is the real part of the equation:

$$z(t) = z_0 e^{-n_c t} cos\omega_0 t \tag{31}$$

It is quite interesting to see the system now oscillating with the frequency $\omega_0 = \Omega\sqrt{1-\zeta^2}$ inside a decaying envelope of $e^{-n_c t}$.

A.2.2. Critically Damped System ($n_c = \Omega$, $\zeta = 1$)

The critically damped oscillator is a special case and has only one solution.

$$\gamma = -n_c \tag{32}$$

As it becomes obvious in the equation

$$z(t) = z_0 e^{-n_c t} \tag{33}$$

no oscillating term is left and hence the deflection will return to the resting state without oscillation. In addition, the critically damped system is the fastest way for a vibration to return to its initial state.

A.2.3. Heavily Damped System ($n_c > \Omega$, $\zeta > 1$)

Heavy damping will force the system to return to its resting position very slowly as observed by solving the following equations. Since now the damping coefficient exceeds the eigenfrequency and ζ becomes greater than 1, the value of the square root is a positive number, and hence the results for

$$\gamma_{1,2} = -n_c \pm \sqrt{n_c^2 - \Omega^2} \tag{34}$$

are all real numbers. The linear combination has to take all the possible solutions into account and depends on initial conditions.

$$z(t) = Ae^{\gamma_1 t} + Be^{\gamma_2 t} \tag{35}$$

Fig. A.2 shows quite well how relaxation time increases with higher damping ratios.

A.3. Driven Damped Resonator

Any driven system (Fig. A.1c) will give in to the frequency of the driving force $F(t)$ with amplitude F_0 but will change in amplitude z_0 depending on the relation between driving frequency ω and the systems eigenfrequency Ω.

$$|z_0| = \frac{\frac{F_o}{m}}{\sqrt{(\Omega^2 - \omega^2)^2 + 4\omega^2\zeta^2\Omega^2}}. \tag{36}$$

In addition to the change in amplitude the system will show a shift in phase

$$arg(z_0) = \varphi = arctan\frac{2\zeta\Omega\omega}{\omega^2 - \Omega^2} \tag{37}$$

which yields the general real solution for the driven system

$$z(t) = \frac{\frac{F_o}{m}}{\sqrt{(\Omega^2 - \omega^2)^2 + 4\omega^2\zeta^2\Omega^2}} cos(\omega t + \varphi). \tag{38}$$

By rearranging the equation a little bit one obtains

$$|z_0| = \frac{\frac{F_o}{k}}{\sqrt{(1 - (\frac{\omega}{\Omega})^2)^2 + 4\zeta^2(\frac{\omega}{\Omega})^2}} \tag{39}$$

$$arg(z_0) = \varphi = arctan\frac{2\zeta(\frac{\omega}{\Omega})}{1 - (\frac{\omega}{\Omega})^2} \tag{40}$$

and the so called gain or amplitude response can be extract of the system.

$$\delta z_0 = \frac{1}{\sqrt{(1 - (\frac{\omega}{\Omega})^2)^2 + 4\zeta^2(\frac{\omega}{\Omega})^2}} \tag{41}$$

Fig. A.3 shows the gain of a driven damped harmonic oscillator with different degrees of damping. The phase shifts immediately by π at resonance frequency for under-critically damped systems and shifts more slowly for bigger damping ratios. What can also be

observed in the figure is that for higher damping ratios the peak smooths up and the resonance frequency shifts to a lower value.

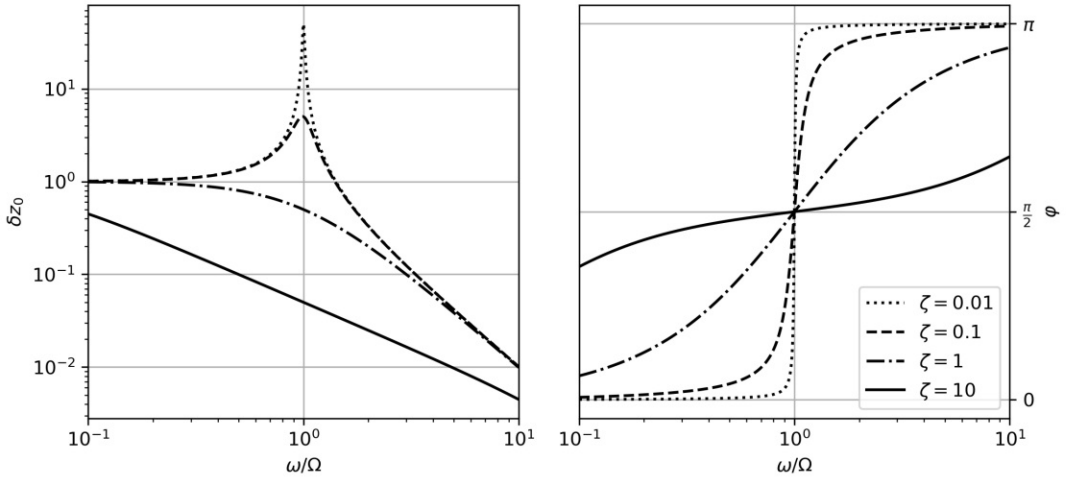

Fig. A.3 Amplitude response and phase shift for different values of ζ.

The resonance frequency is defined as

$$\omega_r = \Omega\sqrt{1 - 2\zeta^2} \tag{42}$$

A.4. Galerkin's Method

In relation to continuum mechanical resonators, Galerkin's method is often used to simplify such a system by reducing the problem to a lumped element model [6]. The method is going to be applied on (18), as also seen here:

$$\rho A\frac{\partial^2 u(x,t)}{\partial t^2} + C\frac{\partial u(x,t)}{\partial t} - \sigma A\frac{\partial^2 u(x,t)}{\partial x^2} = Cv_{air}(t) \tag{43}$$

Following the instructions from the source "Fundamentals of Nanomechanical Resonators" [6], it can be assumed that the string is only resonating at one vibrational mode at a time. Knowing that $u(x,t) = u_n(t)\phi_n(x)$, each term in the equation is multiplied by $\phi_n(x)$, and then integrated over the length of the string ($\int_0^L$). The solution of the first term equals the effective mass of the system:

$$m_{\text{eff},n} = \rho A\int_0^L \phi_n^2(x)dx \tag{44}$$

In case of a string resonator the effective mass equals half the initial mass of the system, therefore, $m_{\text{eff},n} = \frac{1}{2}m_0$.

In order to solve the damping term we extend it by $\frac{\rho A}{\rho A}$:

$$c_{\text{eff},n} = \frac{C}{\rho A} \cdot m_{\text{eff},n} = \frac{C}{\rho A} \cdot \rho A \int_0^L \phi_n^2(x)dx \tag{45}$$

Since $2n_c = \frac{c_{\text{eff},n}}{m_{\text{eff},n}}$, we can also write $2n_c = \frac{C}{\rho A}$.

To solve the third term the mode shape is assumed to be $\phi_n(x) = \phi_0 sin(\beta_n x)$. Hence the second derivative of $\phi_n(x)$ equals $\phi_n''(x) = -\beta_n^2 \phi_n(x)$. Multiplying by $\frac{\rho}{\rho}$ the solution is

$$k_{\text{eff},n} = \frac{\sigma}{\rho}\beta_n^2 \cdot m_{\text{eff},n} = \frac{\sigma}{\rho}\beta_n^2 \cdot \rho A \int_0^L \phi_n^2(x)dx. \tag{46}$$

For $\Omega_n^2 = \frac{k_{\text{eff},n}}{m_{\text{eff},n}}$ we get $\Omega_n^2 = \frac{\sigma}{\rho}\beta_n^2$ as a solution for the system's eigenfrequency. Finally, by setting the driving force zero to get an undriven but damped system, the former continuum mechanical resonator can be expressed in terms of a lumped element model.

$$\frac{\partial^2 u(t)}{\partial t^2} + \underbrace{\frac{C}{\rho A}}_{2n_c} \frac{\partial u(t)}{\partial t} + \underbrace{\frac{\sigma}{\rho}\beta_n^2}_{\Omega_n^2} u(t) = 0 \tag{47}$$

All terms were reduced by the effective mass $m_{\text{eff},n}$.

B. Acoustics

Acoustics addresses the mechanisms of how sound is created, propagated and detected. Sound waves can be separated into different domains, which are split according to the human capability of hearing frequencies from 20 Hz to 20 kHz. Waves with frequencies below 20 Hz are classified as infrasonic, and those above the audible threshold of 20 kHz are classified as ultrasonic as visualized in Fig. B.1 [13].

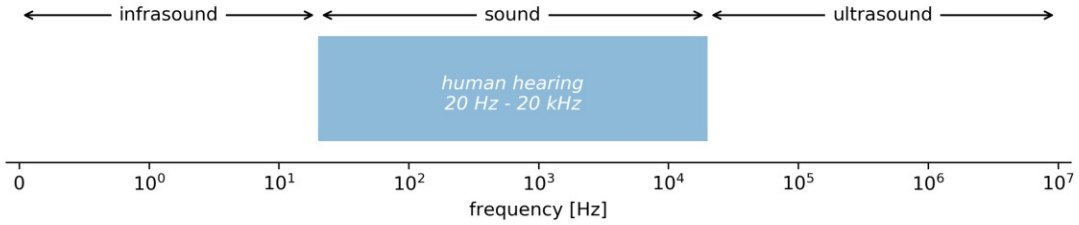

Fig. B.1 Acoustic frequency domains over logarithmic scale.

Acoustic waves can be distinguished between harmonic tones, sound, noise or sound pulses, which show unique characteristics in both time and frequency domain.

Tones are harmonic oscillations with constant or slow changing amplitude. The pitch is dependent on the oscillation frequency and the amplitude defines the sound pressure level SPL (Fig. B.2).

Sound is a periodical, but not simply sinusoidal oscillation, consisting of multiple sine and cosine oscillations. The frequency spectrum shows the different frequency components and their contribution by amplitude (Fig. B.3).

Noise characteristically is an aperiodic oscillation with temporal changing amplitude and fourier components, mostly covering broad frequency ranges (Fig. B.4).

Sound pulses are oscillations of a broad frequency spectrum with fast decaying amplitudes (Fig. B.5)

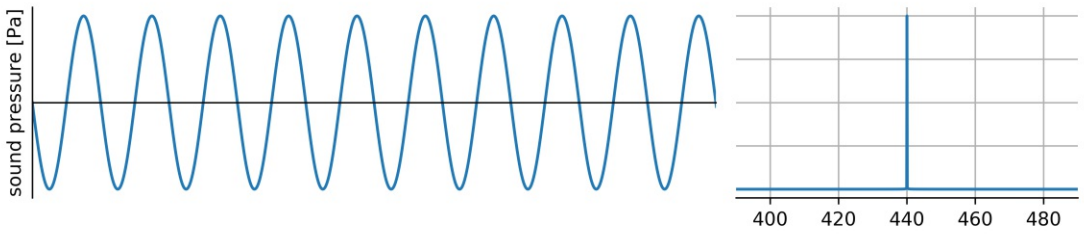

Fig. B.2 Harmonic single frequency tone oscillation.

Fig. B.3 Sound wave of three frequencies.

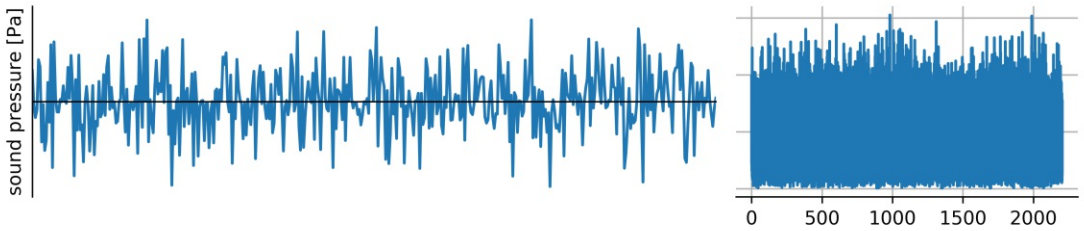

Fig. B.4 Random noise signal.

Fig. B.5 Sound pulse.

B.1. Sound

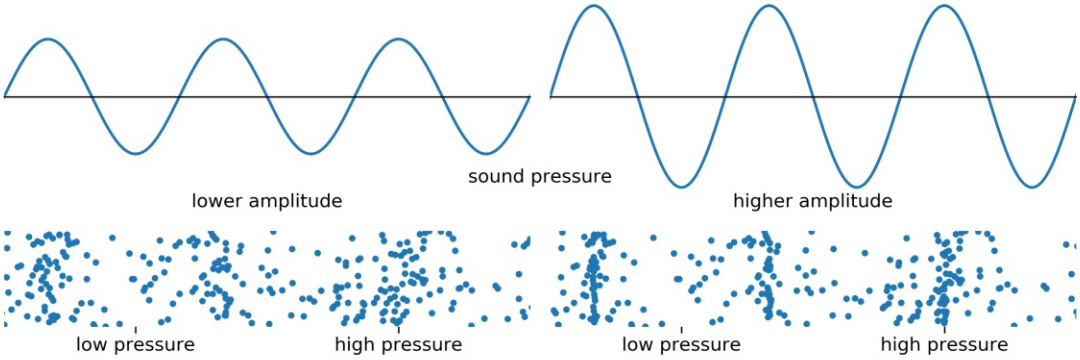

Fig. B.6 Sound wave acting as pressure wave.

Sound is a mechanical wave. Different from electromagnetic waves like light, mechanical waves require a medium to propagate from one location to another. This includes gases, fluids, solids and plasma. While the sound wave propagates through air, the air particles are displaced back and forth colliding with each other, passing their energy to the next one before they bounce back in place. These oscillations around their mean position result in changes of local pressure, particle density and particle velocity. The quantities in (48) consist of the base pressure p_0, base particle density ρ_0 and base particle velocity v_0 part, and the oscillating part $p_\sim$, $\rho_\sim$ and $v_\sim$ induced by the sound wave. It might be important to note that there is a major difference between the speed of sound and the particle velocity. While the speed of sound describes the velocity of the sound waves propagation from point A to point B, the particle velocity refers to the velocity of the particle with which it is oscillating around its mean position. The mean particle velocity depends on the amplitude of the particle's displacement and the frequency of the wave. A higher frequency requires the particle to oscillate faster around its mean position.

$$\begin{aligned} p &= p_0 + p_\sim \\ \rho &= \rho_0 + \rho_\sim \\ v &= v_0 + v_\sim \end{aligned} \tag{48}$$

In gases and fluids the acoustic waves propagate in form of longitudinal waves. This means the displacement of the particles around their mean position takes place in the same direction the wave travels. This is different to light waves, where the magnetic

and the electric field oscillate perpendicular to the vector of propagation. While the particles are oscillating back and forth there will be areas of higher particle density and areas of lower particle density. Hence denser locations will result in higher pressure and the less dense locations will result in a lower pressure compared to the general air pressure. Therefore sound is a pressure wave. Demonstrated in Fig. B.6, the amplitude of the particle displacement decides how tight the air particles are pushed together by the sound wave, resulting in a change of loudness or sound pressure level.

B.2. Derivation of Sound Quantities

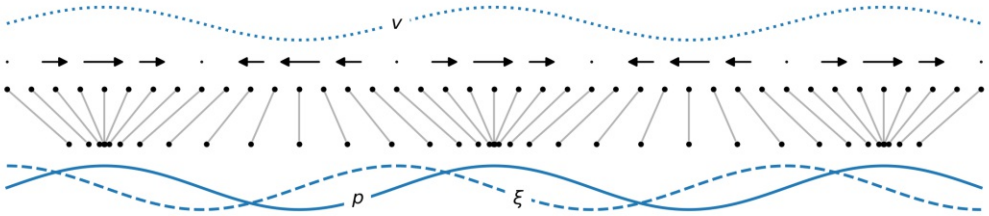

Fig. B.7 Visualization of sound pressure p, particle displacement ξ and particle velocity v.

As already mentioned, an acoustic wave is the displacement of particles from their resting position. For a harmonic wave the displacement of a particle on position z and time t is described by

$$\begin{aligned} \xi(t,z) &= A \cdot cos(\omega t - kz) \\ &= \xi_0 \cdot cos(\omega t - kz) \end{aligned} \tag{49}$$

and the time derivation returns the particle's velocity

$$v(t,z) = \frac{\partial \xi}{\partial t} = -\omega \cdot \xi_0 \cdot sin(\omega t - kz). \tag{50}$$

The maximum value of the particle's velocity is given by:

$$v_0 = \omega \cdot \xi_0. \tag{51}$$

In comparison, sound pressure is derived by:

$$p(t,z) = -\rho c^2 \frac{\partial \xi}{\partial x} = -\rho c^2 k \cdot \xi_0 \cdot sin(\omega t - kz). \tag{52}$$

B.3. Acoustic Sensors

The basic concept of an acoustic sensor is to transform the acoustic quantity into an electric signal. As seen in Fig. B.7, several quantities of the sound field are provided, though mainly the sound pressure and the particle velocity are used for sound detection. Even though sound pressure and sound velocity move in phase and the amplitudes are proportional to each other, the two quantities differ in a major characteristic. While pressure is a local quantity given by the density of air particles at this particular measuring point, the particle velocity as a vector carries the information of the direction from which the sound wave approached the sensor.

Pressure microphones are designed to transduce local sound pressure into an electrical signal. They usually consist of a membrane responding to the incoming sound waves. Early inventions like the carbon microphone measured changes in electrical resistance using carbon particles between two electrodes, which where compressed and released by the fluctuating sound pressure. This concept is highly outdated due to high noise and low frequency response.

Dynamic microphones use electrical conductors inducing voltage while moving in a magnetic field. Moving coil microphones pick up changes in sound pressure via a membrane, which moves a coil through a magnetic field. This principle is widely used in macroscopic microphone designs.

Another representative for dynamic microphones is the ribbon microphone. An extremely thin conductive ribbon picks up sound waves with a figure-of-eight directionality. The ribbon microphone oscillates inside a magnetic field which induces a voltage used for the transduction.

Condenser microphones consist of two electrodes forming a condenser. One is the membrane and the other one is hidden inside the microphone's capsule. Changes in the membrane's deflection are measurable as a changing capacity of the condenser. The electret microphone is a variation of this concept using a permanently polarized membrane instead of the bias voltage a regular condenser microphone would need. Condenser type microphones are the state of the art regarding miniaturization. Thanks to sophisticated semiconductor fabrication technology they represent the vast majority of MEMS microphones nowadays [14].

C. Supporting Graphics

C.1. Yield

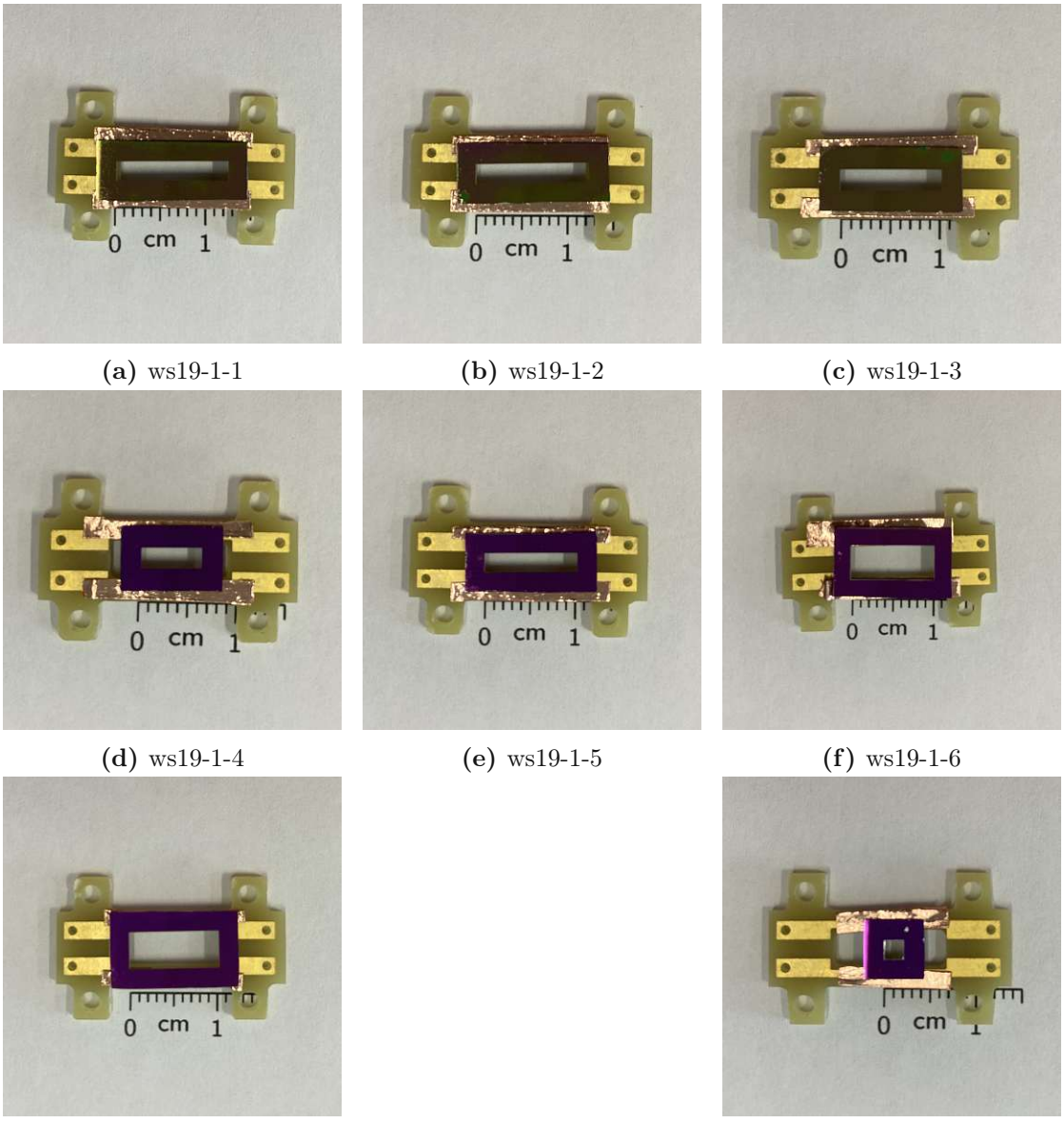

(a) ws19-1-1 **(b)** ws19-1-2 **(c)** ws19-1-3

(d) ws19-1-4 **(e)** ws19-1-5 **(f)** ws19-1-6

(g) ws19-1-7 **(h)** ws19-1-9

Fig. C.1 Samples mounted on PCB for safer and faster handling. String is not visible in the pictures.

C.2. Total Harmonic Distortion

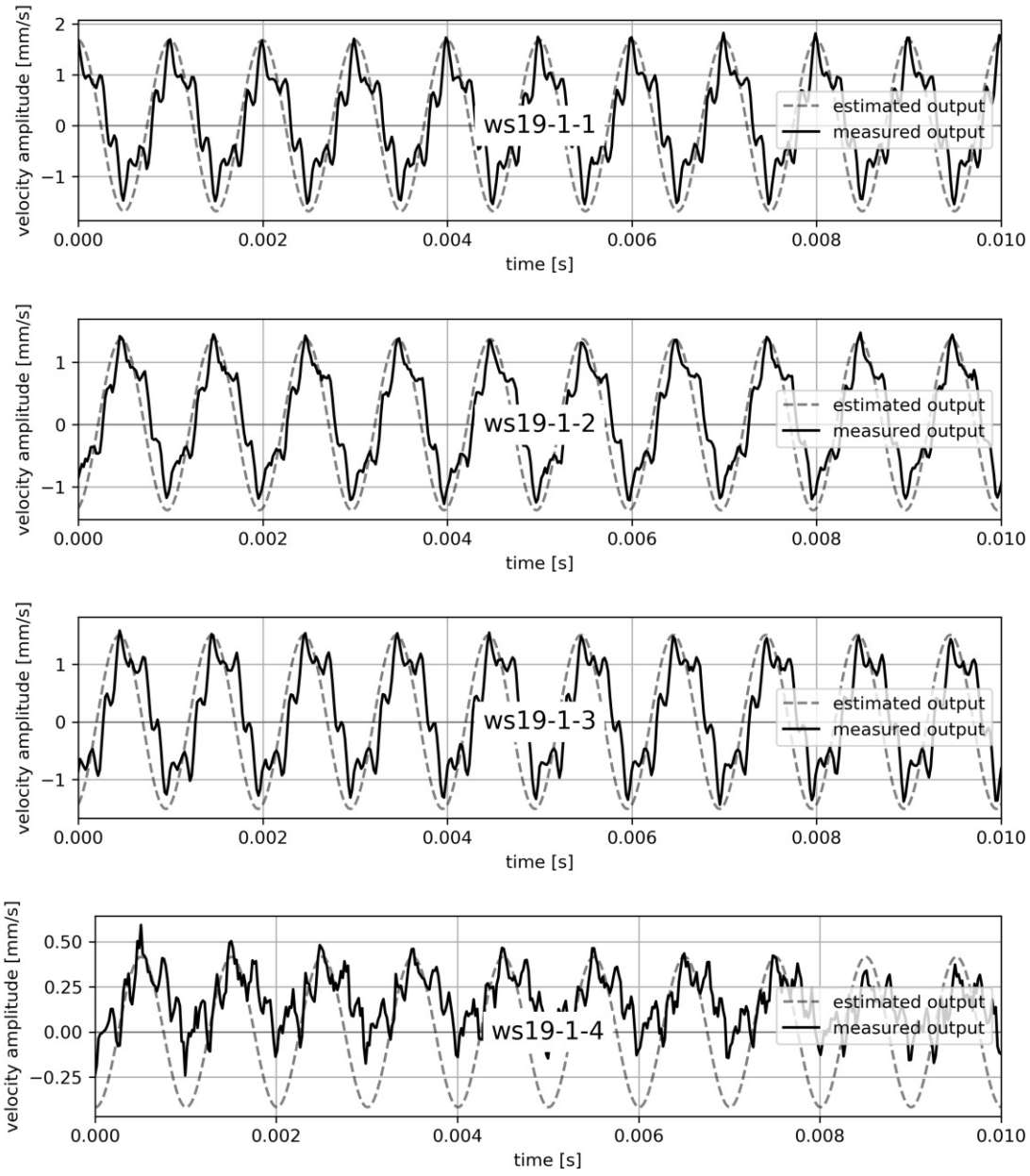

Fig. C.2 Total harmonic distortion for samples ws19-1-1 to ws19-1-4.

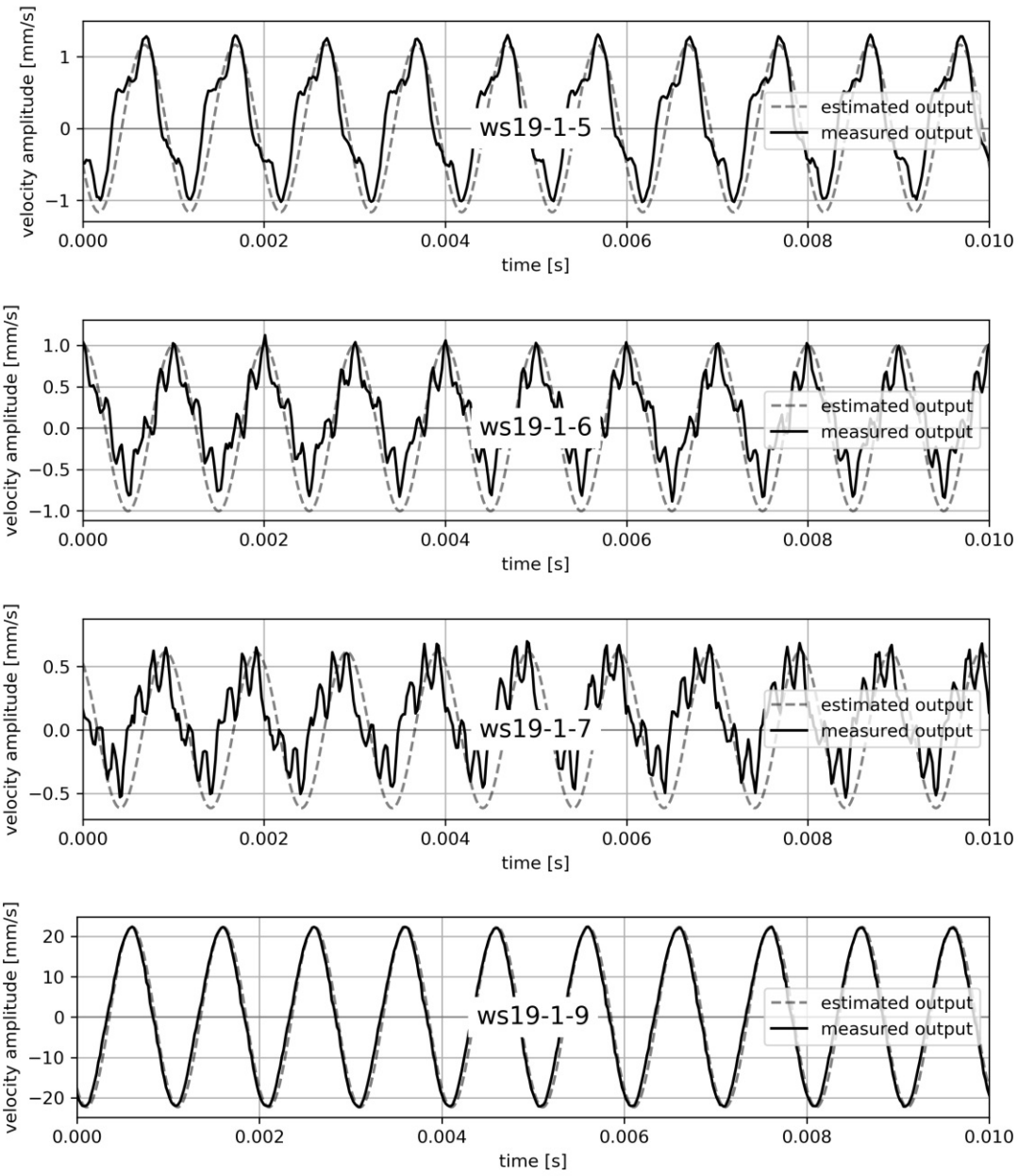

Fig. C.3 Total harmonic distortion for samples ws19-1-5 to ws19-1-9.

C.3. Frequency Response

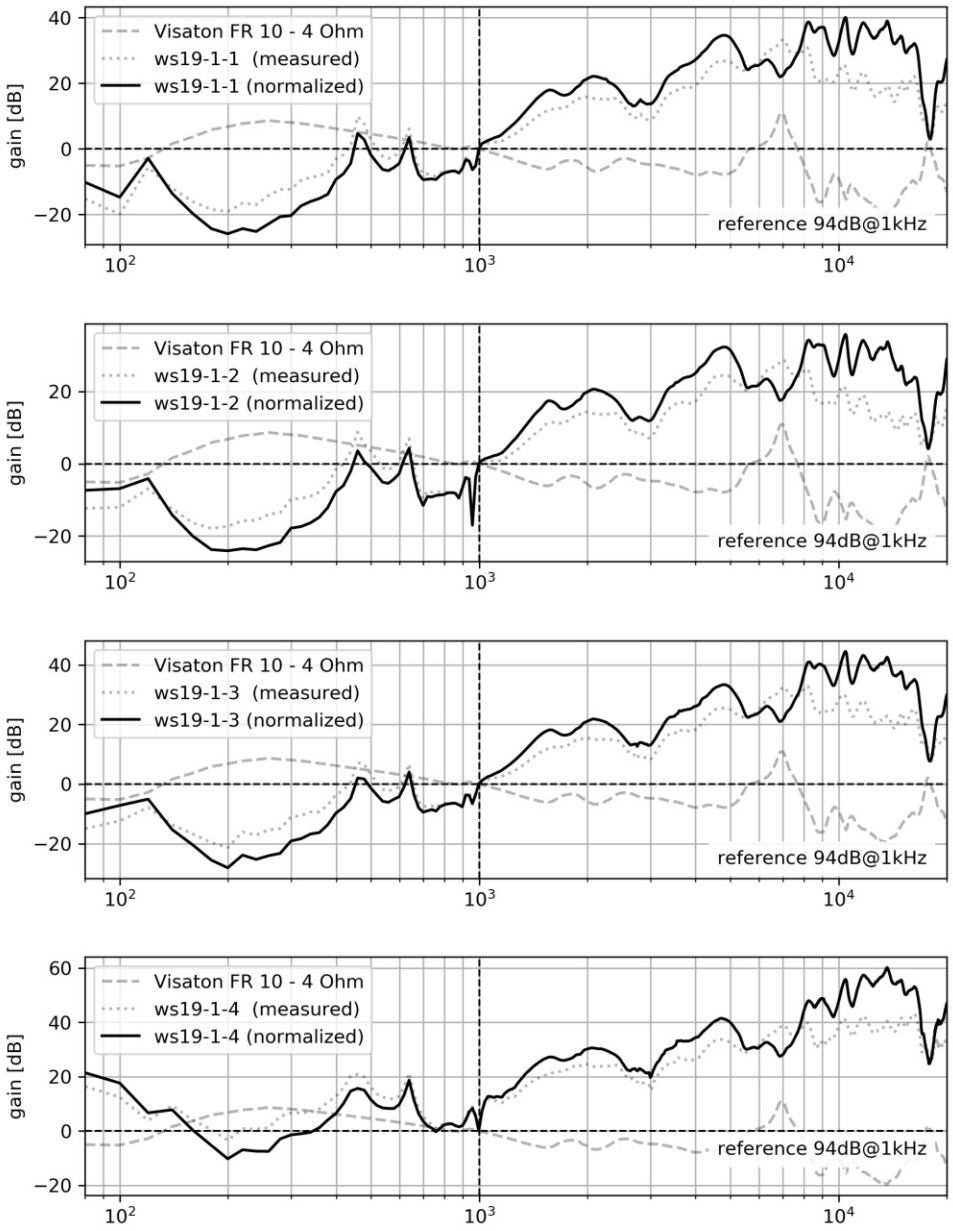

Fig. C.4 Frequency response for samples ws19-1-1 (top) to ws19-1-4 (bottom). Due to a difficult experimental setup the curve does not provide a reliable statement. Normalized to 1 kHz.

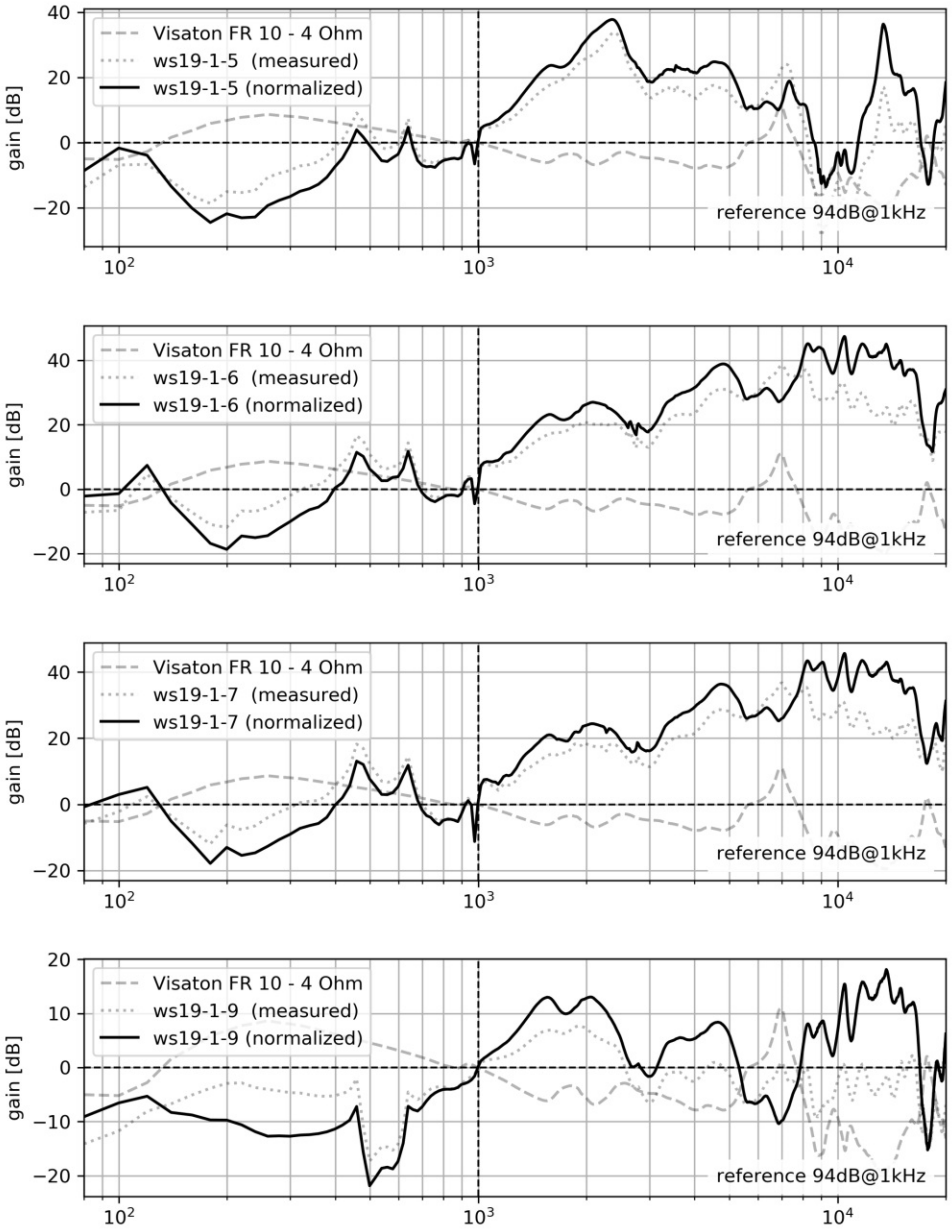

Fig. C.5 Frequency response for samples ws19-1-5 (top) to ws19-1-9 (bottom). Due to a difficult experimental setup the curve does not provide a reliable statement. Normalized to 1 kHz.

C.4. Directionality

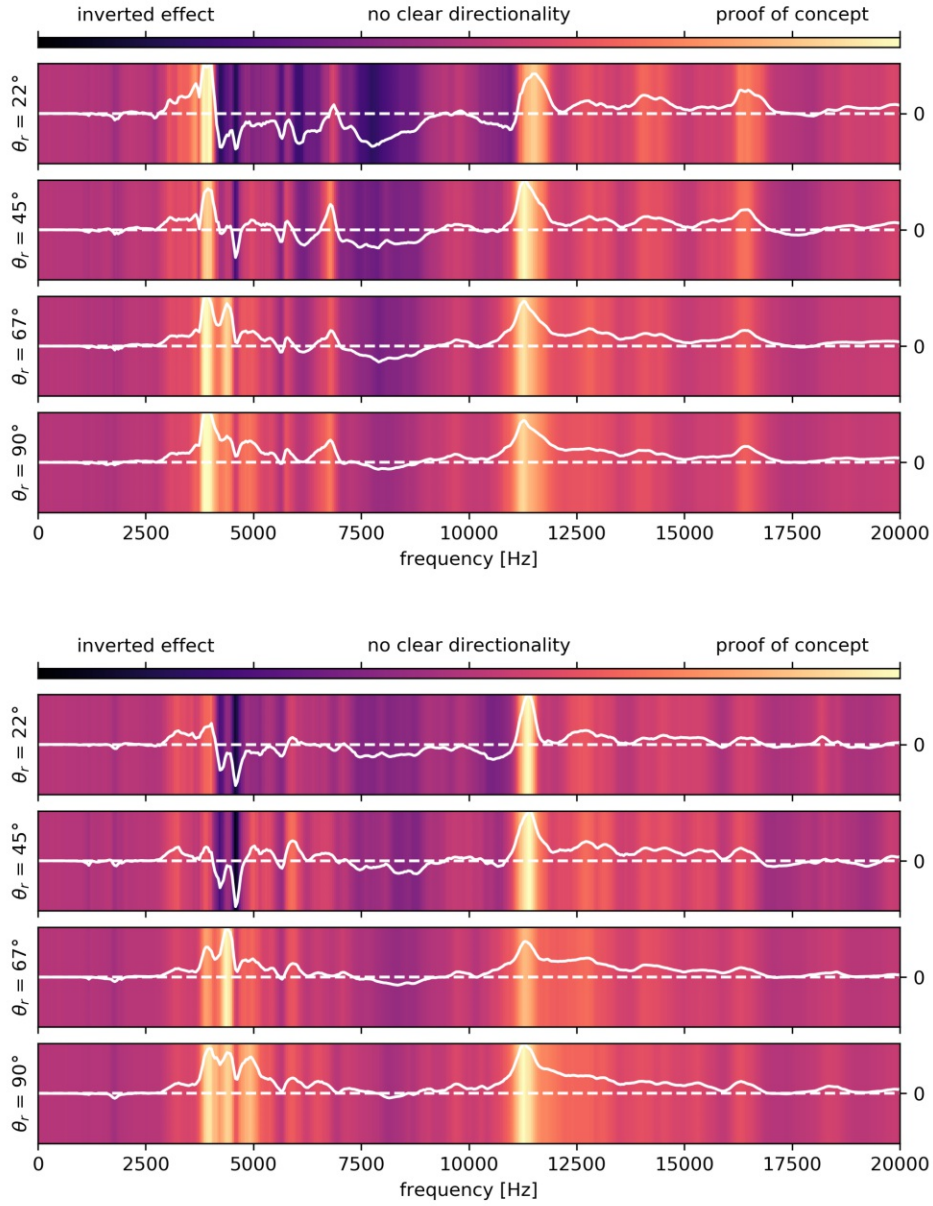

Fig. C.6 Directional response for different angles of actuation θ_r in relation to direct actuation $\theta_r = 0$ for ws19-1-2 (top) and ws19-1-3 (bottom). The graphs show that the predicted directionality is not consistent along the audible frequency range.

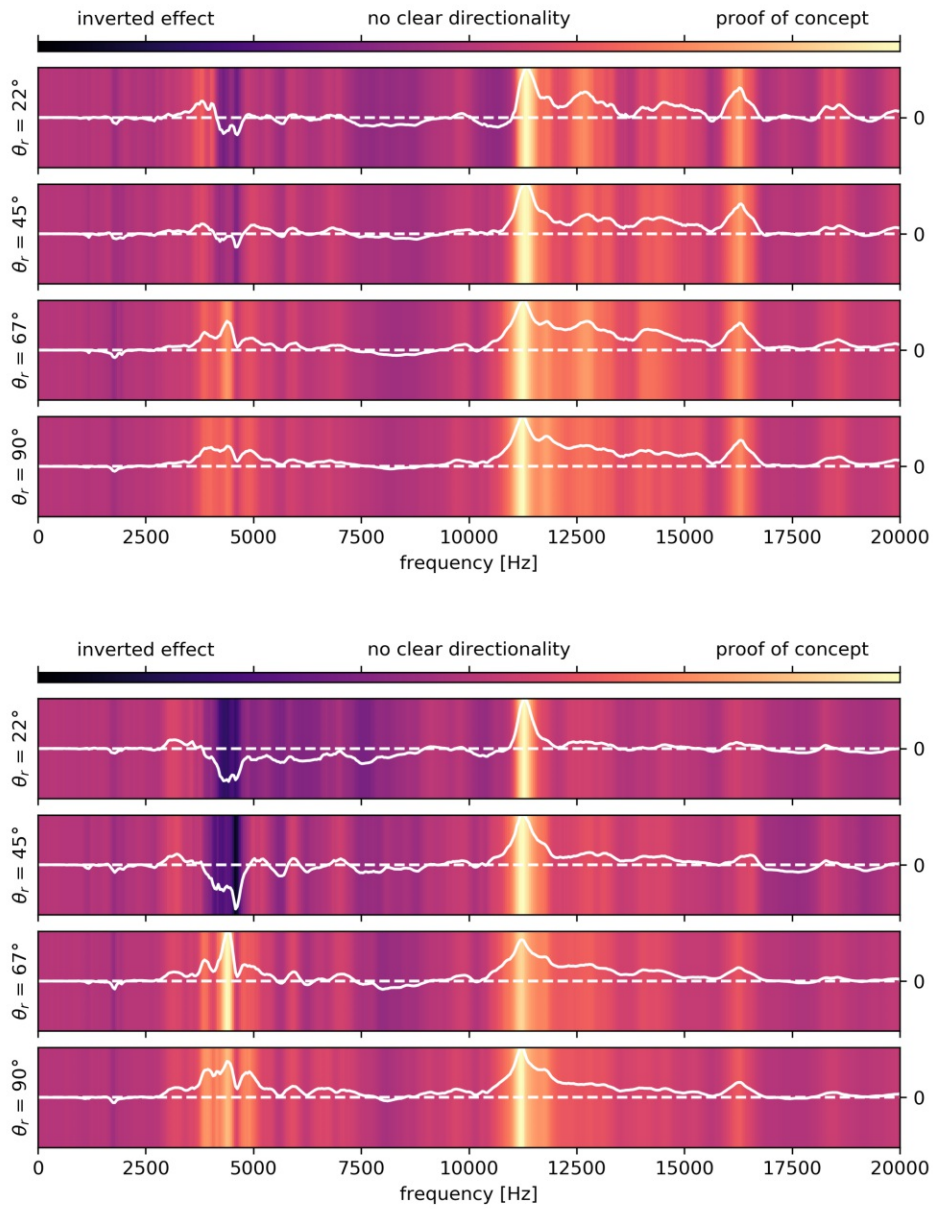

Fig. C.7 Directional response for different angles of actuation θ_r in relation to direct actuation $\theta_r = 0$ for ws19-1-4 (top) and ws19-1-7 (bottom). The graphs show that the predicted directionality is not consistent along the audible frequency range.

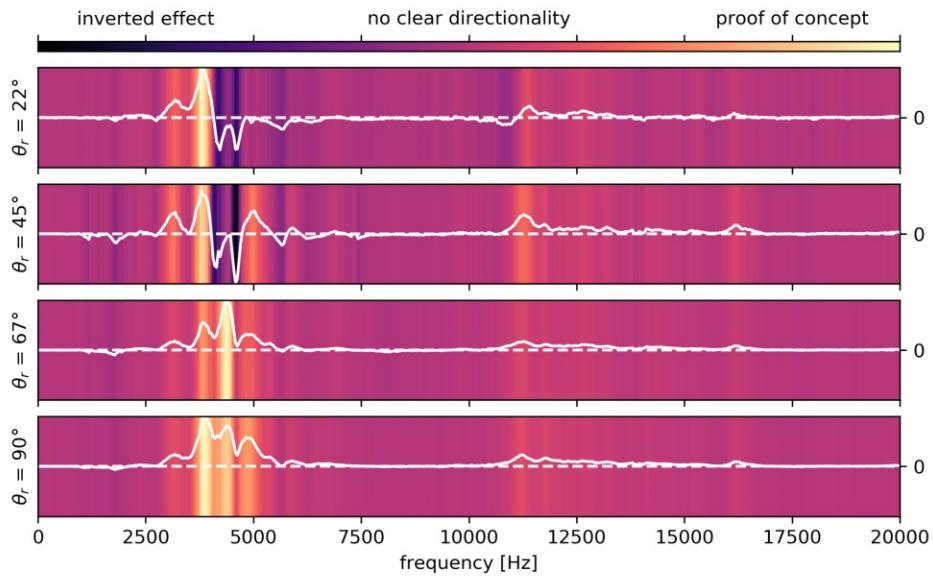

Fig. C.8 Directional response for different angles of actuation θ_r in relation to direct actuation $\theta_r = 0$ for ws19-1-9. The graphs show that the predicted directionality is not consistent along the audible frequency range.

C.5. Recording

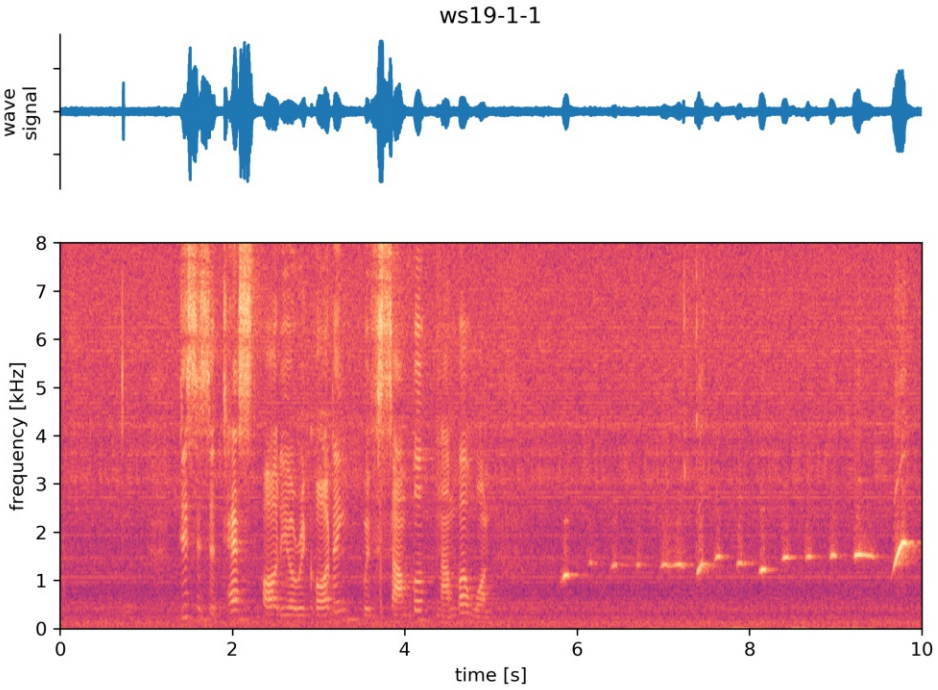

Fig. C.9 Clear talking from 1 m distance: "This is a test audio recording with sample number one (whistling)" In the background at a low responsive angle the adjacent vacuum pump from another experiment, usually operating somewhere around 1 kHz, is also audible.

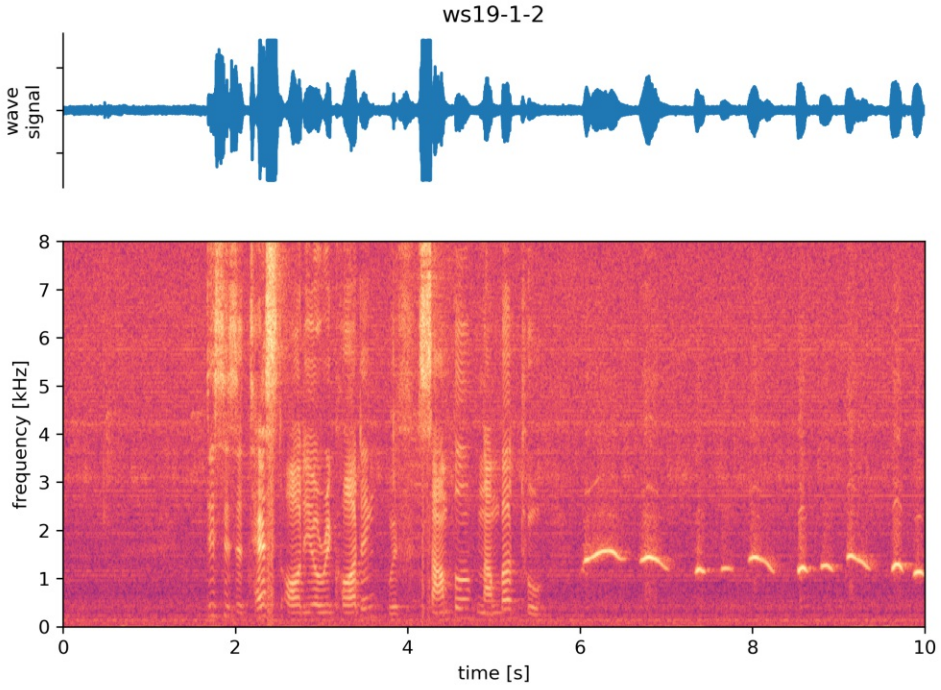

Fig. C.10 Clear talking from 1 m distance: "This is a test audio recording with sample number two (whistling)" In the background at a low responsive angle the adjacent vacuum pump from another experiment, usually operating somewhere around 1 kHz, is also audible.

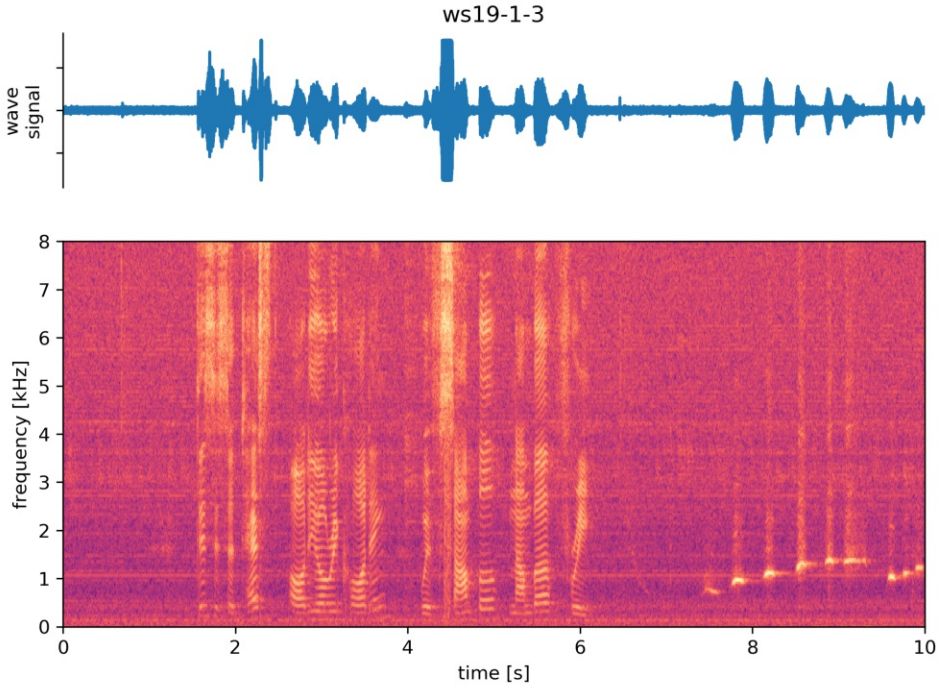

Fig. C.11 Clear talking from 1 m distance: "This is a test audio recording with sample number three (whistling)" In the background at a low responsive angle the adjacent vacuum pump from another experiment, usually operating somewhere around 1 kHz, is also audible.

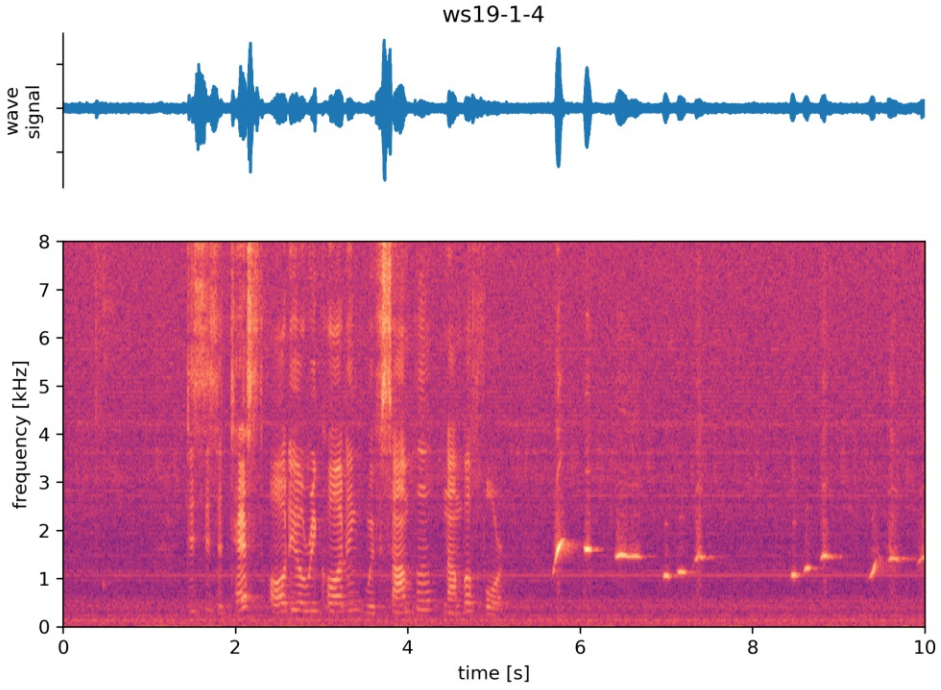

Fig. C.12 Clear talking from 1 m distance: "This is a test audio recording with sample number four (whistling)" In the background at a low responsive angle the adjacent vacuum pump from another experiment, usually operating somewhere around 1 kHz, is also audible.

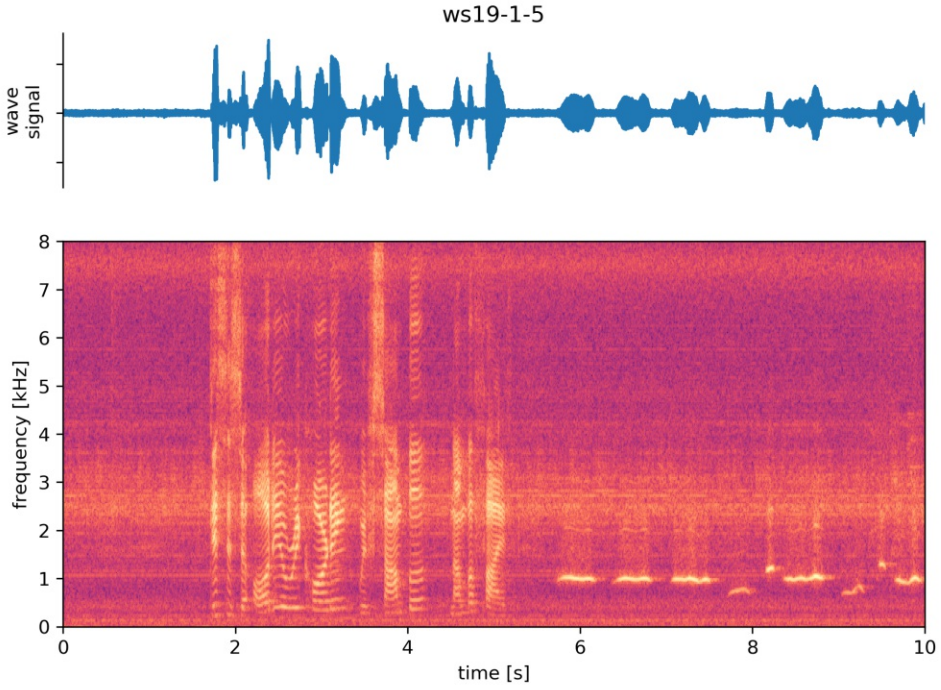

Fig. C.13 Clear talking from 1 m distance: "This is a audio recording with sample number five (whistling)" In the background at a low responsive angle the adjacent vacuum pump from another experiment, usually operating somewhere around 1 kHz, is also audible. This recording shows a much higher noise level but is still clearly audible. It also seems to have a slight distortion to the voice speaking.

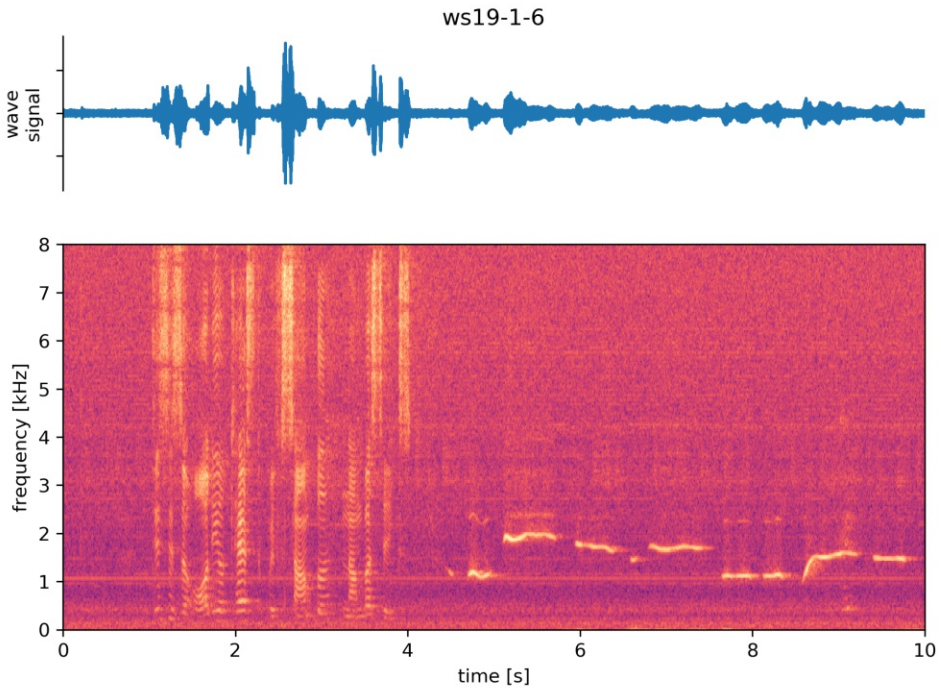

Fig. C.14 Clear talking from 1 m distance: "This is a audio recording with sample number six (whistling)" In the background at a low responsive angle the adjacent vacuum pump from another experiment, usually operating somewhere around 1 kHz, is also audible. The recording seems to have less distortion than the previous ones (1-5).

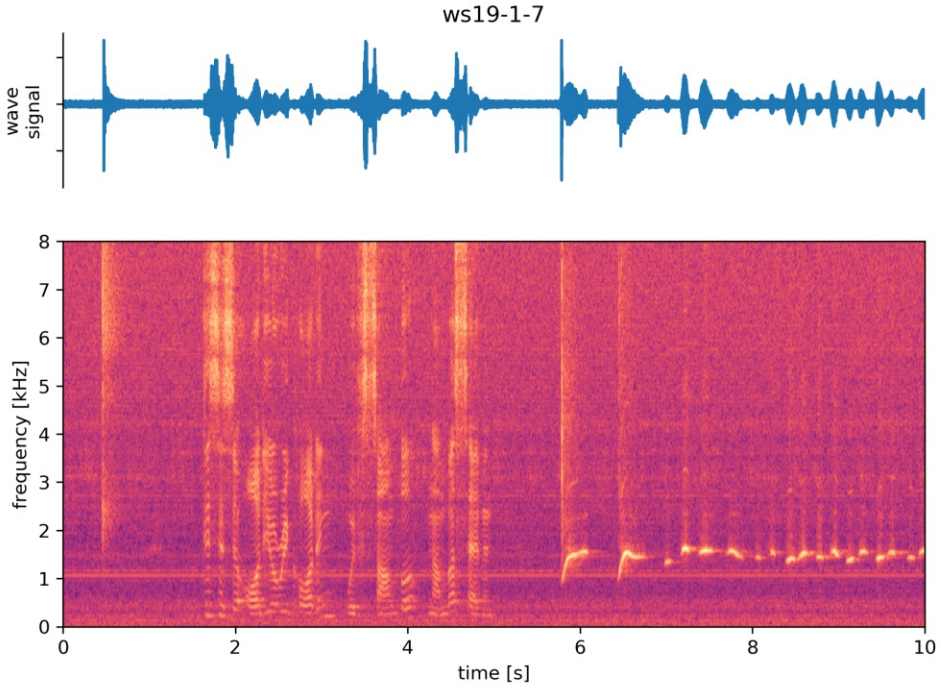

Fig. C.15 Clear talking from 1 m distance: "This is a audio recording with sample number seven (whistling)" In the background at a low responsive angle the adjacent vacuum pump from another experiment, usually operating somewhere around 1 kHz, is also audible. The recording (just like 6) seems to have less distortion that the previous ones (1-5).

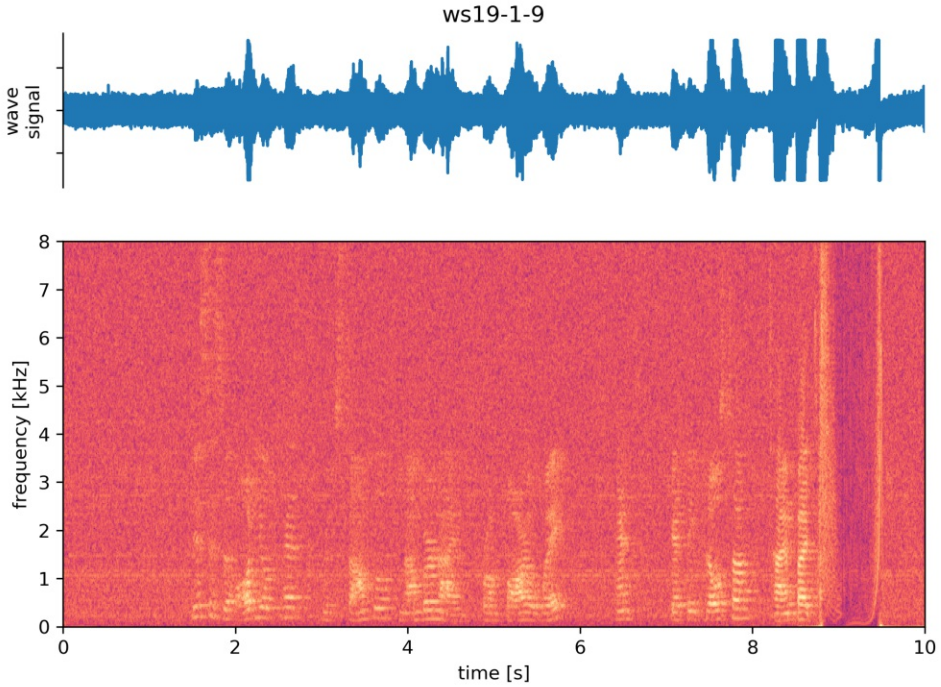

Fig. C.16 Clear talking from 5 m distance down to 1 m distance: "This is a audio test with sample number nine from far away and getting closer as time goes by (sample chirps as the voice is close and drives the sample too hard)" In the background at an low responsive angle the adjacent vacuum pump from another experiment, usually operating somewhere around 1 kHz, is also audible.

D. References

[1] Jian Zhou and Ronald N. Miles. "Sensing fluctuating airflow with spider silk". In: *Proceedings of the National Academy of Sciences* 114.46 (Oct. 2017), pp. 12120–12125. DOI: 10.1073/pnas.1710559114. URL: https://doi.org/10.1073%2Fpnas.1710559114.

[2] Jian Zhou and Ronald N. Miles. "Directional Sound Detection by Sensing Acoustic Flow". In: *IEEE Sensors Letters* 2.2 (June 2018), pp. 1–4. DOI: 10.1109/lsens.2018.2843376. URL: https://doi.org/10.1109%2Flsens.2018.2843376.

[3] Jian Zhou et al. "Highly-damped nanofiber mesh for ultrasensitive broadband acoustic flow detection". In: *Journal of Micromechanics and Microengineering* 28.9 (May 2018), p. 095003. DOI: 10.1088/1361-6439/aac2f5. URL: https://doi.org/10.1088%2F1361-6439%2Faac2f5.

[4] Ronald N. Miles et al. "A flow-sensing velocity microphone". In: *2019 IEEE SENSORS*. IEEE, Oct. 2019. DOI: 10.1109/sensors43011.2019.8956947. URL: https://doi.org/10.1109%2Fsensors43011.2019.8956947.

[5] Minhang Bao. "Air Damping". In: *Analysis and Design Principles of MEMS Devices*. Elsevier, 2005, pp. 115–174. DOI: 10.1016/b978-044451616-9/50004-7. URL: https://doi.org/10.1016%2Fb978-044451616-9%2F50004-7.

[6] Silvan Schmid, Luis Guillermo Villanueva, and Michael Lee Roukes. "Effective Parameters". In: *Fundamentals of Nanomechanical Resonators*. Springer International Publishing, 2016, pp. 38–40. DOI: 10.1007/978-3-319-28691-4_1. URL: https://doi.org/10.1007%2F978-3-319-28691-4_1.

[7] Jerad Lewis. *Understanding Microphone Sensitivity*. URL: https://www.analog.com/en/analog-dialogue/articles/understanding-microphone-sensitivity.html. (accessed: 023.08.2021).

[8] NATIONAL INSTRUMENTS CORP. *Understanding Frequency Performance Specifications*. URL: https://www.ni.com/de-at/support/documentation/supplemental/06/understanding-frequency-performance-specifications.html. (accessed: 01.08.2020).

[9] Germany Infineon Technologies AG 81726 Munich. *IM69D130*. URL: https://www.infineon.com/dgdl/Infineon-IM69D130-DS-v01_00-EN.pdf?fileId=5546d462602a9dc801607a0e46511a2e. (accessed: 01.08.2020).

[10] Wikipedia. *Total Harmonic Distortion — Wikipedia, die freie Enzyklopädie*. [Online; Stand 23. August 2021]. 2019. URL: https://de.wikipedia.org/w/index.php?title=Total_Harmonic_Distortion&oldid=193886146.

[11] Niklas Luhmann et al. "Effect of oxygen plasma on nanomechanical silicon nitride resonators". In: *Applied Physics Letters* 111.6 (Aug. 2017), p. 063103. DOI: 10.1063/1.4989775. URL: https://doi.org/10.1063%2F1.4989775.

[12] Silvan Schmid, Luis Guillermo Villanueva, and Michael Lee Roukes. "Resonance Frequency". In: *Fundamentals of Nanomechanical Resonators*. Springer International Publishing, 2016, pp. 1–56. DOI: 10.1007/978-3-319-28691-4_1. URL: https://doi.org/10.1007%2F978-3-319-28691-4_1.

[13] Heinrich Kuttruff. *Acoustics - An Introduction*. Taylor & Francis, 2006. ISBN: 0-203-97089-6.

[14] Ao.Univ.Prof. Dipl.-Ing. Dr.techn. Keplinger Franz. "Sensorik". Lecture Documents. TU Wien LVA 366.051 Sensorik für MS.